

1 **Whole-mantle tomography of Southeast Asia: New insight into plumes and slabs**

2 **Genti Toyokuni^{1*}, Dapeng Zhao¹, and Kenkichi Kurata¹**

3 ¹ Department of Geophysics, Graduate School of Science, Tohoku University, Sendai 980-8578,
4 Japan

5 Submitted to *Journal of Geophysical Research: Solid Earth* in February 2022

6 *Corresponding author:

7 Genti Toyokuni

8 E-mail: toyokuni@tohoku.ac.jp

9 ORCID ID: 0000-0003-3786-207X

10

11 **Key Points:**

- 12 • A novel high-resolution P-wave tomographic model of the entire mantle beneath
13 Southeast Asia is obtained.
- 14 • The model reveals a continuous whole-mantle plume beneath the Hainan hotspot rising
15 from the core-mantle boundary.
- 16 • A strong low-velocity anomaly exists beneath the Australian slab, which may reflect
17 subduction-induced hot mantle upwelling.

18

19 **Abstract**

20 We present detailed 3-D images of whole mantle P-wave velocity structure beneath Southeast
21 Asia and surrounding regions. The results are obtained by applying an updated global
22 tomographic method to invert ~8 million P, pP, PP, PcP, and Pdiff arrival times from 23,587
23 earthquakes recorded at 14,136 stations distributed all over the world. Our tomographic model
24 reveals a continuous, thin low-velocity (low-V) zone from the surface to the core-mantle
25 boundary beneath the Hainan hotspot, which may reflect the Hainan plume that exists in the
26 whole mantle. Beneath the Australian slab that has subducted into the lower mantle, a strong
27 low-V anomaly is detected, which may reflect slab hot mantle upwelling (SHMU) due to
28 return flow of the slab subduction. Our model also shows the distinct shape of subducted slabs in
29 the upper mantle and slab remnants in the lower mantle. In particular, a hole in the subducting
30 Australian slab is revealed at depths of 280–430 km beneath eastern Java. The low-V anomaly in
31 the mantle wedge above the Australian slab is connected with the SHMU through the slab hole,
32 suggesting that mixture of the island arc magma and the SHMU may have caused huge eruptions
33 of the Tambora and Rinjani volcanoes in eastern Java.

34 **Plain Language Summary**

35 Southeast Asia is surrounded by plate subduction zones, and very intense seismic and volcanic
36 activities have been occurring there. Volcanic activity originating from the deep Earth,
37 represented by the Hainan hotspot, also takes place. It is known that seafloor spreading and
38 subduction have been repeated in the past, and the relationship between the slabs subducted
39 deeply into the mantle and the plate movement on the surface is an important key to
40 understanding the evolution history of this region. In this study, we apply an updated method of
41 seismic tomography to investigate the whole mantle 3-D P-wave velocity structure beneath SE

42 Asia. For the first time, a continuous whole-mantle plume is revealed beneath the Hainan hotspot
43 with its root at the core-mantle boundary. Hot mantle upwellings above and below the
44 subducting Australian slab are connected through a slab hole at depths of 280–430 km beneath
45 eastern Java. The mixture of those hot mantle materials might have caused huge eruptions of the
46 Tambora and Rinjani volcanoes in eastern Java.

47 **1. Introduction**

48 Southeast (SE) Asia and its surrounding regions exhibit very complex structure and tectonics,
49 where the Sunda Plate, Eurasian Plate, Philippine Sea Plate, Indian Plate, Australian Plate, and
50 several small plates are interacting with each other (Figure 1). The Sunda Plate located in the
51 center of the region constitutes land areas such as the Indochina Peninsula, Malay Peninsula,
52 Indonesian islands (Sumatra, Java, Borneo, etc.), the Philippines, and broad oceanic areas such
53 as the Sunda Shelf, the South China Sea (SCS), the Sulu Sea, and the Celebes Sea. The Sunda
54 Plate is surrounded by well-developed subduction zones. Trenches of particular note are the
55 Sunda Trench where the Indian Plate and the Australian Plate are subducting beneath the Sunda
56 Plate from the west and the south, respectively, the Philippine Trench where the Philippine Sea
57 Plate subducts beneath the Sunda Plate from the east, and the Manila Trench where the Sunda
58 Plate subducts beneath the Philippine Sea Plate from the west.

59 Seismic activity in this region is extremely high, and many large earthquakes have occurred
60 at depths < 100 km along the Sunda Trench and the Philippine Trench (Figure S1). In particular,
61 the 2004 Sumatra–Andaman earthquake (Mw 9.1) that occurred on December 26, 2004 caused
62 230,000 deaths due to the strong ground motion and tsunami. Deep-focus earthquakes also
63 occurred actively, and the June 17, 1996 earthquake off Maumere, Indonesia, recorded Mw 7.9
64 despite its focal depth of 587 km. Activity of arc volcanoes making up the volcanic front is also

65 high in this region. For example, the Tambora volcano on Sumbawa Island, east of Java, caused
66 the world's largest volcanic eruption in the recorded history on April 5, 1815, which resulted in
67 "the year without a summer." Furthermore, there are hotspot volcanoes on Hainan Island in the
68 northern part of the SCS, and inland volcanic activity is also high around the Indochina
69 Peninsula (Figure 1).

70 The tectonic evolution of SE Asia after 350 Ma can be summarized as four-stage separation
71 of continental slivers from the Gondwana continent on the southern side, and their accretion to
72 the Eurasia continent on the northern side (Metcalf, 2005; Müller et al., 2019). At the first stage
73 (the Devonian, 350 Ma), continental slivers consisted of North China, South China, Tarim,
74 Indochina, East Malaya, and West Sumatra were separated from Gondwana and drifted
75 northwards, resulted in opening of the Paleo-Tethys on the southern side. At the second stage
76 (the Lower Permian, 270 Ma), continental slivers consisted of Sibumasu and Qiangtang drifted
77 northwards, resulted in opening of the Meso-Tethys on the southern side and closure of the
78 Paleo-Tethys on the northern side by the Late Triassic. At the third stage (the Late Triassic, 200
79 Ma), continental slivers consisted of Lhasa, West Burma, West Sulawesi, etc. drifted northwards,
80 resulted in opening of the Cenozoic Tethys on the southern side and closure of the Meso-Tethys on
81 the northern side by the Early Cretaceous. At the fourth stage (the Late Jurassic, 140 Ma), the
82 Indian subcontinent drifted northwards, resulted in opening of the Indian Ocean on the southern
83 side and closure of the Cenozoic Tethys on the northern side by the Eocene. At 40 Ma, the Indian
84 subcontinent began to collide with the Eurasian continent, the SCS expanded, and the Sunda
85 Plate rotated clockwise. Through these histories, from the east, the Izu Plate subducted until
86 60 Ma, followed by subduction of the Pacific Plate, the Paleo-South China Sea Plate, and the
87 Philippine Sea Plate, etc.

88 Seismic tomography is a powerful tool to obtain detailed 3-D images of the subsurface
89 structure. Tomographic studies targeting SE Asia have been actively made, but most of them
90 focused on the upper mantle structure (Filippova & Solovey, 2021; Hua et al., 2022; Huang et al.,
91 2015; Lebedev & Nolet, 2003; Legendre et al., 2015; Li & van der Hilst, 2010; Li et al., 2006;
92 Shi et al., 2020; Wehner et al., 2021; Wei et al., 2012; Widiyantoro et al., 2011; Zenonos et al.,
93 2019). The lower mantle structure beneath SE Asia has been mainly studied by global seismic
94 tomography (e.g., Hall & Spakman, 2015). The following is an overview of the structural
95 features obtained by previous tomographic studies regarding the upper and lower mantle beneath
96 this area. More detailed reviews can be found in Zhao (2015) and Hall & Spakman (2015).

97 Regarding the upper mantle structure, detailed studies have been conducted by mainly using
98 P-wave velocity (V_p) regional tomography (Hua et al., 2022; Huang et al., 2015; Li & van der
99 Hilst, 2010; Li et al., 2006; Shi et al., 2020; Wei et al., 2012; Widiyantoro et al., 2011; Zenonos
100 et al., 2019). Regional tomographic studies using surface-wave and S -wave data have been also
101 conducted, but the resolution of the obtained S -wave velocity (V_s) models is lower than that of
102 the V_p models (Filippova & Solovey, 2021; Lebedev & Nolet, 2003; Legendre et al., 2015;
103 Zenonos et al., 2019). Recently, Wehner et al. (2021) determined a 3-D V_s model under SE Asia
104 using full waveform tomography. To date, very few studies have revealed the detailed upper
105 mantle structure using global tomography (Pesicek et al., 2008; Zhao et al., 2021). There are also
106 some studies combining the tomographic results with tectonic reconstruction models or mantle
107 convection simulation (Hafkenscheid et al., 2001; Hall & Spakman, 2015; Jolivet et al., 2018;
108 Spakman & Hall, 2010; Yang et al., 2016; Zahirovic et al., 2016).

109 A common feature of the upper mantle tomography is that the subducting slabs are clearly
110 imaged as high-velocity (high- V) zones where intermediate-depth and deep earthquakes occurred.

111 The Indo-Australian slab subducting from the Sunda Trench has been investigated in detail at
112 depths ≤ 660 km. Of particular interest are the bending of the slab beneath northern Sumatra
113 (Hall & Spakman, 2015; Pesicek et al., 2008) and the presence of a slab hole with a diameter of
114 ~ 400 km at 250–500 km depths beneath eastern Java (Hall & Spakman, 2015; Wehner et al.,
115 2021; Widiyantoro et al., 2011; Zenonos et al., 2019). Huang et al. (2015) conducted Vp
116 anisotropic tomography and suggested the existence of 3-D mantle flow through the slab hole,
117 but they showed that the slab hole was located between Sumatra and Java. Wehner et al. (2021)
118 mentioned the relationship of the slab hole with the nearby Tambora volcano, but they did not
119 discuss about its eruption mechanism. Other characteristic slab structures include a spoon-shaped
120 bended slab beneath the Banda Sea (Spakman & Hall, 2010), and the Sangihe and Halmahera
121 slabs that sink subparallel to each other with a north-south strike beneath the Molucca Sea (Hall
122 & Spakman, 2015; Huang et al., 2015). The continental lithosphere of the Sunda Plate
123 surrounded by these subduction systems is generally imaged as low-velocity (low-V) zones in all
124 tomographic models.

125 Many global tomography models have been used to investigate the lower mantle structure
126 beneath SE Asia (e.g., Amaru, 2007; Burdick et al., 2017; Fukao & Obayashi, 2013; Hosseini,
127 2016; Hosseini et al., 2020; Lu et al., 2019; Obayashi et al., 2013; Simmons et al., 2010, 2012;
128 Zhao, 2004; Zhao et al., 2013). However, the spatial resolution of these models is generally $>$
129 ~ 500 km, which is inferior to that of regional tomography. Zhao et al. (2021) applied a global
130 tomography method with spatial resolution comparable to that of regional tomography to South
131 China–Indochina–SCS areas, but their model does not cover most of SE Asia.

132 A common feature of the lower mantle tomography is the existence of a high-V body beneath
133 the Sunda Shelf–Borneo–Philippines at depths ~ 900 –1400 km. This body is identified as slab

134 remnants subducted in the Paleogene by studies combined with plate reconstructions (Hall &
135 Spakman, 2015; Replumaz et al., 2004), but no study has been made to investigate the
136 correspondence between the detailed slab shape and the time-dependent position of the
137 subduction zones. Most of the tomographic studies have revealed a hot mantle plume beneath the
138 Hainan hotspot rising from the lower mantle. However, the continuity of this plume in the lower
139 mantle is unclear in the existing models, and the depth at which the plume began to rise is
140 controversial (e.g., Hua et al., 2022; Huang et al., 2015; Yan et al., 2018; Zhao et al., 2021).

141 As outlined above, SE Asia has grown through repeating subductions and formations of
142 various tectonic plates, and contains important clues to elucidate subduction dynamics and
143 evolution of the Earth. However, previous studies using high-resolution seismic tomography had
144 focused mainly on the upper mantle structure, and very few studies focused on the detailed
145 whole-mantle structure beneath SE Asia. The purpose of this work is to obtain a high-resolution
146 3-D Vp model of the whole mantle, from the lithosphere to the core-mantle boundary (CMB),
147 beneath entire SE Asia using an updated global tomography method, so as to improve our
148 understanding of the deep structure and mantle dynamics of this region, in particular, the
149 subducting slabs and upwelling mantle plumes.

150 **2. Method**

151 Global tomography is a method to image 3-D seismic velocity structure of the whole Earth
152 by inverting a great number of travel-time data of earthquakes recorded at seismic stations
153 distributed all over the world (Zhao, 2015). In this work, we use the global tomography method
154 proposed by Zhao (2004) and updated by Zhao et al. (2013, 2017). Zhao et al. (1992) and Zhao
155 (2004) developed a method that can trace seismic rays for an Earth model with 3-D velocity
156 variations and complex shapes of velocity boundaries (such as the Moho, 410 and 660 km

157 discontinuities). The unknown parameters to be inverted are velocity perturbations from an
 158 initial 1-D model at 3-D grid nodes that are arranged along the latitude and longitude lines. [Zhao](#)
 159 [et al. \(2013\)](#) updated their tomographic code by adopting a so-called flexible grid that is
 160 independent of the latitude and longitude so that the 3-D mantle structure beneath the polar
 161 regions can be also imaged well. [Zhao et al. \(2017\)](#) further proposed a multiscale grid approach
 162 that adopts the 3-D flexible grid for the whole globe but reduces the grid interval beneath a target
 163 region. This multiscale global tomography method is able to investigate the whole mantle 3-D
 164 structure beneath the target area with high resolution comparable to that of regional tomography.
 165 [Zhao et al. \(2017\)](#) applied this updated method to the Izu-Bonin area to investigate the detailed
 166 geometry and structure of the subducted Pacific slab in and around the source zone of the 2015
 167 Bonin deep earthquake (M7.9, focal depth ~680 km). This method was further applied to image
 168 the whole-mantle structure beneath Greenland and its surroundings ([Toyokuni et al., 2020](#)) and
 169 the South China–Indochina–SCS region ([Zhao et al., 2021](#)).

170 Here we apply this multiscale tomographic method ([Zhao et al., 2017](#)) to SE Asia. The
 171 absolute travel-time residuals from the i th event to the j th station (t_{ij}) is defined as

$$t_{ij} = T_{ij}^{\text{OBS}} - T_{ij}^{\text{CAL}} \quad (1)$$

172
 173
 174 where T_{ij}^{OBS} and T_{ij}^{CAL} are the observed and calculated (theoretical) arrival times, respectively.
 175 T_{ij}^{CAL} is calculated by using a 3-D ray tracing technique that combines the pseudo-bending
 176 scheme ([Um & Thurber, 1987](#)) and Snell's law ([Zhao et al., 1992](#)). The initial 1-D model is the
 177 IASP91 Earth model ([Kennett & Engdahl, 1991](#)). We conduct the tomographic inversions using
 178 the LSQR algorithm ([Paige & Saunders, 1982](#)) with damping and smoothing regularizations. The

179 optimal values of the damping parameter ($\lambda_d = 15$) and smoothing parameters ($\lambda_{sv} = 1.05 \times$
180 10^{-2} and $\lambda_{sh} = 9 \times 10^{-3}$ for the vertical and horizontal directions, respectively) are found from
181 trade-off curves that are constructed by conducting many inversions with various pairs of the
182 damping and smoothing parameters, following the previous studies (Toyokuni et al., 2020; Zhao
183 et al., 2017, 2021).

184 The target region spans the latitudinal range of $[-20^\circ, 25^\circ]$, longitudinal range of $[90^\circ, 140^\circ]$,
185 and depth range of [0 to 2889 km] (from the surface to CMB). The horizontal grid interval is set
186 to be fine as 55.6 km inside the target area (a great-circle distance of 0.5° on the surface) and to
187 be coarse as 222.2 km outside the target area (a great-circle distance 2.0° on the surface) (Figure
188 2a). The grid meshes are placed at the following depths inside the target volume: 15, 32.5, 50, 75,
189 100, 140, 180, 220, 260, 300, 340, 380, 420, 460, 500, 575, 650, 725, 800, 875, 950, 1025, 1100,
190 1200, 1300, 1400, 1500, 1600, 1700, 1800, 1900, 2000, 2100, 2200, 2300, 2425, 2550, 2675, and
191 2800 km, and outside the target volume: 15, 50, 100, 180, 260, 340, 420, 500, 650, 800, 950,
192 1100, 1300, 1500, 1700, 1900, 2100, 2300, 2550, and 2800 km (Figure 2b). The number of
193 horizontal grid nodes at each depth is shown in Table S1.

194 3. Data

195 The data used in this study are arrival times of not only direct P waves, but also four types of
196 later phases, i.e., pP, PP, PcP, and Pdiff (Figure S2). The data are obtained from the International
197 Seismological Centre (ISC) website (<http://www.isc.ac.uk/>) and further selected for analysis. (1)
198 The data from 1964 to 2016 in the ISC-EHB catalog (<http://www.isc.ac.uk/isc-ehb/>) are
199 downloaded, and only the earthquakes containing P, pP, and PP arrival times are extracted. We
200 note that the ISC-EHB catalog does not contain PcP and Pdiff arrival times. The number of
201 extracted earthquakes is 170,435. (2) The data from 2002 to 2012 in the reviewed ISC catalog

202 (<http://www.isc.ac.uk/iscbulletin/>) are downloaded, and only the earthquakes containing PcP and
203 Pdiff arrival times are extracted. The number of extracted earthquakes is 72,191. (3) To
204 homogenize the hypocentral distribution of 242,626 earthquakes, which are the sum of the data
205 (1) and (2), the entire crust and mantle are divided into small cubic blocks, and in each block
206 only one earthquake with the largest number of arrival times is extracted. The number of
207 earthquakes in the study volume is enhanced by adopting a smaller block size of 0.8° (horizontal)
208 $\times 10$ km (depth) inside the target volume, and a larger block size of 1.5° (horizontal) $\times 20$ km
209 (depth) outside the target volume. The data with travel-time residuals exceeding ± 5 s are not
210 used in the tomographic inversion. The number of earthquakes finally used is 23,587, and the
211 total number of arrival time data is 7,762,801, consisting of 7,200,864 P, 246,856 pP, 207,728 PP,
212 70,253 PcP, 37,100 Pdiff arrival times, which were recorded at 14,136 seismic stations (Figure
213 3). The number of earthquakes and stations inside the target volume is 11,344 and 656,
214 respectively (Figures S3 and S4). The focal depth range of the extracted earthquakes inside the
215 study volume is 0–700 km.

216 The CPU time for one tomographic inversion of the selected data set is approximately 43 h
217 and 23 min using our workstation computer Xeon E5-2660 v3 (2.6 GHz, 1 core). The root-mean-
218 square (RMS) travel-time residual is 1.67 s for the initial 1-D Vp model, but it is reduced to 1.37
219 s for the final 3-D Vp model obtained by the inversion with the optimal damping and smoothing
220 parameters as mentioned above.

221 4. Results

222 Figure S5 shows the seismic ray coverage in various depth layers. The density of ray path
223 coverage varies throughout the study volume, which can be visualized by ray hit counts (HC),
224 i.e., the number of rays sampling a grid node (Figures S6–S8). To illustrate the HC distribution,

225 areas with $HC < 50$, $50 \leq HC < 100$, and $HC \geq 100$ are shown in black, gray, and white,
226 respectively. Robust results are expected in areas with a $HC \geq 50$, and less reliable parts are
227 masked in white in the tomographic images. Near the Earth's surface (depth ≤ 180 km), seismic
228 rays do not crisscross well beneath the Pacific Ocean, SCS, and Indian Ocean. At greater depths,
229 the ray density and crisscrossing beneath the Pacific Ocean and SCS improves, while the sparse
230 rays beneath the Indian Ocean does not improve until the bottom of the mantle transition zone
231 (MTZ, 410–660 km depths). In the lower mantle (depth > 660 km), rays crisscross well down to
232 the CMB. The reference velocity model is optimized by subtracting the average velocity
233 perturbation at each depth from the velocity anomalies obtained using IASP91 (Kennett &
234 Engdahl, 1991) (Figure 4). Here we show our tomographic results as V_p perturbations from the
235 optimized 1-D model (Figures 5–8), while the V_p images relative to the original IASP91 model
236 are shown in Figures S9–S11.

237 The results are shown in map views in Figures 5 and 6. The corresponding HC distributions
238 are shown in Figure S6. At a depth of 100 km, high- V_p bands along the Sunda, Manila, and
239 Philippine Trenches, and subduction zone at the eastern end of the Banda Sea Plate are
240 prominent, which clearly correspond to the subducting oceanic slabs. Almost the entire region
241 beneath the northern Australian Craton is also imaged as a remarkable high- V_p zone. Spot-like
242 high- V_p zones are visible at the boundary between the Indian and Australian Plates. As for low-
243 V_p anomalies, a wide extent is observed inside the subduction zones such as beneath the Java
244 Sea, Sulu Sea, Celebes Sea, Banda Sea, Sunda Shelf, and Borneo Island. Spot-like low- V_p zones
245 are also visible at the southern end of the Yangtze Plate and beneath the joint of the Malay
246 Peninsula. At depths of 250–400 km, the high- V_p bands corresponding to the subducting slabs
247 move further behind the trenches as they subduct deeper. Beneath eastern Java, there is a

248 prominent break (window) of the high-Vp band at depths > 280 km. The high-Vp zones beneath
249 northern Australia and the boundary between the Indian and Australian Plates disappear with
250 increasing depth. The low-Vp anomalies inside the subduction zones become less prominent at
251 greater depths, but instead, other low-Vp zones appear outside the Sunda Trench. Especially,
252 beneath the Timor Sea, a low-Vp band elongated in the east-west direction is remarkable. A low-
253 Vp zone is visible at all depths beneath the northern end of the Sunda Plate, i.e., beneath
254 southern Yangtze Plate–Hainan hotspot–Indochina Peninsula.

255 At depths of 430–520 km, high-Vp zones beneath the Andaman Sea, SCS, and the western
256 end of the Caroline Plate are prominent. The break of the high-Vp band beneath eastern Java is
257 still visible at depths of 430–460 km. A remarkable low-Vp anomaly appears beneath from
258 southern SCS to Borneo, but it disappears with increasing depth. The low-Vp band outside the
259 Sunda Trench is further expanded, and the low-Vp amplitudes become particularly remarkable at
260 its southwestern part. The low-Vp zone beneath the northern end of the Sunda Plate is confined
261 around Hainan Island. Spot-like low-Vp zones are also visible beneath the active volcanoes on
262 the central Philippine Sea Plate. At depths of 550–650 km, a vast high-Vp zone appears beneath
263 the Sunda Plate. Other high-Vp zones also widely exist beneath the Philippine Sea Plate and
264 Australian Plate, so high-Vp amplitudes dominate almost the entire study area. On the other
265 hand, low-Vp is only prominent at the vast crescent-shaped zone beneath the southwestern Sunda
266 Trench. Other low-Vp features remain just as spot-like, for example, beneath Hainan Island.

267 At depths of 700–800 km, the high-Vp zones become less noticeable, and they remain only
268 beneath the Malay Peninsula, Sumatra, Java, and the west of the Philippine Sea Plate. Instead, a
269 vast low-Vp anomaly appears beneath Hainan–SCS–Sunda Shelf–Borneo. The crescent-shaped
270 low-Vp zone beneath the southwestern Sunda Trench can be seen at all depths. At depths of

271 900–1400 km, a vast high-Vp zone appears beneath the Sunda shelf–Borneo–Philippines with
272 the largest amplitudes at depths of 1000–1100 km. However, the high-Vp amplitudes gradually
273 decrease at greater depths, and at a depth of 1400 km, only a slight trace remains beneath Borneo.
274 The crescent-shaped low-Vp zone beneath the southwestern Sunda Trench is still visible at
275 depths of 900–1000 km, but is subdivided into spot-like low-Vp zones at greater depths. Spot-
276 like low-Vp zones are also visible beneath Hainan Island and its surrounding areas.

277 At depths of 1500–2400 km, both the high-Vp and low-Vp amplitudes become small, and
278 only a few conspicuous features are visible. A weak high-Vp anomaly is found beneath the
279 Philippine Sea Plate at depths of 1800–2000 km. Spot-like low-Vp zones exist beneath the
280 southwest of the Sunda Trench only at depths of 1500–1600 km. A confined low-Vp anomaly
281 exists beneath around Hainan Island at depths of 1500–2200 km, while it moves toward the
282 southeast as the depth increases. At depths of 2600–2800 km, both the high-Vp and low-Vp
283 amplitudes increase again, indicating that the structural heterogeneity is stronger at these depths
284 compared to the shallower areas. A prominent high-Vp band exists beneath from the east of
285 Borneo to the Philippine Sea Plate. On the other hand, a low-Vp band is remarkable beneath the
286 Timor Sea. Spot-like low-Vp anomalies can be seen beneath the western margin of the
287 Philippine Sea Plate and beneath the SCS on the CMB.

288 Vertical cross-sections of our Vp tomographic model and the corresponding HC distributions
289 are shown in [Figures 7–8](#) and [Figures S7–S8](#), respectively. In [Figure 7](#), the C–C' to I–I' sections
290 are almost orthogonal to the Sunda subduction zone, and the Australian slab subducting
291 northward from the Sunda Trench is clearly imaged. Among these, the D–D' to H–H' sections
292 show that the slab penetrates the MTZ and sinks to a depth of ~1400 km in the lower mantle. In
293 the G–G' and H–H' sections through the break in the high-Vp subducted Australian slab at depths

294 of 280–460 km beneath eastern Java (Figure 5), no earthquakes have occurred inside the break,
295 suggesting the existence of a hole in the slab. It is consistent with the characteristics of seismicity
296 in other regions of the world, where earthquakes occur in the high-Vp zone, or at the boundary
297 between high-Vp and low-Vp anomalies (Huang & Zhao, 2004; Mishra & Zhao, 2003; Toyokuni
298 et al., 2021; Yang et al., 2022). The D-D' to I-I' sections clearly show low-Vp anomalies in the
299 upper mantle extending toward the volcano located at the volcanic front of the Sunda subduction
300 zone. In the J-J' to L-L' sections orthogonal to the boundary between the Australian and Timor
301 Plates, the subducted Australian slab in the upper mantle can be clearly confirmed (e.g., I-I'
302 section). In these sections, earthquakes occur continuously along the high-Vp slab subducting
303 toward the MTZ. In addition, the J-J' and L-L' sections show the slab subduction at the boundary
304 between the Sunda and Molucca Sea Plates, and at the boundary between the Bird's Head and
305 Banda Sea Plates, respectively. In the M-M' to O-O' sections, a clear high-Vp zone can be
306 confirmed from ~2000 km depth to the CMB beneath the southern part of the Philippine Sea
307 Plate.

308 In Figure 7, the c-c' and d-d' sections passing through the Hainan hotspot show a clear
309 plume-like low-Vp anomaly that rises from the CMB with the modulated low-Vp amplitudes
310 depending on depths. In the f-f' to h-h' sections that are almost orthogonal to the Philippine
311 Trench, the Philippine Sea slab subducting westward beneath the Sunda Plate is clearly imaged
312 as high-Vp anomalies. Especially in the H-H' section, a high-Vp anomaly with the same slope,
313 which seems to be another slab, can be seen in the lower mantle beneath the subducting
314 Philippine Sea slab. This high-Vp zone seems to be sinking to the CMB while rolling back
315 eastward. The K-K' section clearly shows the low-Vp anomaly beneath volcanoes constituting
316 the volcanic front of the Sunda subduction zone and the high-Vp slab beneath it. In the M-M' to

317 O-O' sections, a prominent high-Vp anomaly exists beneath the Australian Craton at depths <
318 ~400 km.

319 In [Figure 8](#), the E-E' and F-F' sections passing through the Hainan hotspot clearly show
320 strong low-Vp anomalies in the upper mantle. Especially in the E-E' section, the low-Vp conduit
321 rising from the CMB is connected with the low-Vp anomaly in the upper mantle, which very
322 likely indicate the Hainan mantle plume. The low-Vp amplitude of the conduit in the E-E'
323 section decreases once at depths around 1000–2000 km, but the low-Vp amplitude in the F-F'
324 section increases at the same depth. These features suggest that this low-Vp conduit rises
325 vertically from the CMB, meanders to the southwest direction at a depth of ~2000 km, and then
326 rises again to the upper mantle where it broadens beneath the Hainan hotspot and Indochina
327 Peninsula.

328 In [Figure 8](#), the G-G' section shows a high-Vp zone that corresponds to the Australian slab
329 subducting from the Sunda Trench and sinking through the MTZ to a depth of ~1500 km. In the
330 H-H' section, this high-Vp anomaly and another high-Vp zone corresponding to the Philippine
331 Sea slab subducting from the Philippine Trench are combined to form a U-shaped high-Vp
332 anomaly. Furthermore, in the I-I' section on the southeastern side, a thin high-Vp zone extending
333 vertically from the bottom of the U-shaped anomaly toward the CMB is clearly imaged. The J-J'
334 section shows a high-Vp pile deposited on the CMB.

335 **5. Resolution tests**

336 We performed three kinds of resolution tests, including the checkerboard resolution tests
337 (CRTs) ([Humphreys & Clayton, 1988](#); [Zhao et al., 2017](#)), restoring resolution tests (RRTs)
338 ([Zhao et al., 1992, 2017](#)), and synthetic resolution tests (SRTs) ([Toyokuni et al., 2020](#); [Zhao et](#)

339 [al., 2017](#)), to evaluate the ray coverage and spatial resolution of our tomographic model. To
340 conduct the CRTs, we construct an input velocity model that contains alternate positive (+3%)
341 and negative (−3%) V_p anomalies assigned to the 3-D grid nodes. Two input models with
342 different grid intervals (CRT1 and CRT2, [Tables 1, S2, and S3](#)) are prepared. To conduct the
343 RRT, we highlight the patterns of the actual tomographic result to construct the RRT input V_p
344 model, i.e., at the grid nodes with the V_p perturbation (dV_p) $> +0.6\%$ in the real tomographic
345 model, we set $dV_p = +1.5\%$, and at the grid nodes with $dV_p < -0.6\%$ in the real tomographic
346 model, we set $dV_p = -1.5\%$ in the RRT input model ([Table 1](#)). V_p perturbations at the other grid
347 nodes are set to zero. To conduct the SRTs, we construct input models with $dV_p = +1.5\%$
348 representing the Australian slab, and $dV_p = -1.5\%$ representing hot mantle upwelling above and
349 beneath the slab and the Hainan mantle plume. Seven SRT input models with different
350 combinations of the high- V_p slab and low- V_p anomalies are constructed (SRT1–SRT7, [Table 1](#)),
351 which are prepared so as to confirm (1) the continuity of the Hainan mantle plume from the
352 surface to CMB, and (2) the reliability of high- V_p Australian slab and a hole in it, low- V_p corner
353 flow in the mantle wedge, low- V_p slab hot mantle upwelling, and low- V_p corridor
354 connecting the two low- V_p sections. Synthetic datasets for the CRT, RRT, and SRT are
355 constructed by calculating theoretical travel times for each input model but with random errors
356 added, which range between -0.2 and $+0.2$ s with a standard deviation of 0.1 s, representing the
357 picking errors of the observed data. In the RRTs and SRTs, we use the same grid setting in the
358 main computation ([Section 2](#)).

359 Main features of the test results are summarized in [Figures 9 and 10](#); the complete test results
360 are shown in the supporting information for the CRT1 ([Figure S12–S14](#)), CRT2 ([Figure](#)
361 [S15–S17](#)), RRT ([Figure S18–S22](#)), SRT1 ([Figure S23–S27](#)), SRT2 ([Figure S28–S32](#)), SRT3

362 (Figure S33–S37), SRT4 (Figure S38–S42), SRT5 (Figure S43–S48), SRT6 (Figure S49–S52),
 363 and SRT7 (Figure S53–S57). Regarding the CRT results, the recovery rate is defined as follows:

$$RR_i (\%) = \frac{(\text{dVp at the } i\text{th node of the output model})}{(\text{dVp at the } i\text{th node of the input model})} \times 100 \quad (2)$$

364

365

366 On the map views of the CRT1 results (Figure S12), the output dVp patterns are biased to
 367 either high-Vp or low-Vp, and the resolution is obviously poor at shallow depths (15–140 km).
 368 As for the recovery rate, the black-to-grey areas with poor recovery are dominant beneath the
 369 Pacific Ocean, SCS, and Indian Ocean at depths of 15–140 km, whereas white areas are
 370 dominant in other parts from the Earth's surface to CMB. In the vertical cross-sections (Figures
 371 S13–S14), the depth extent of the areas with good resolution can be confirmed more clearly,
 372 displaying less severe pattern of reliability shown by the ray hit count (Figures S7–S8). The
 373 CRT2 results (Figures 9a and S15–S17) are slightly severe, and the black-to-grey areas with
 374 poor recovery can be seen beneath the Indian Ocean to a depth of 650 km, although the pattern
 375 shows almost the same reliability indicated by the ray hit count. The two CRT results show that
 376 the whole mantle beneath the study area except for the upper mantle (depths \leq 660 km) beneath
 377 the Indian Ocean, and depths \leq 140 km in other oceanic areas has a lateral resolution of 167 km
 378 and a depth resolution of 40–75 km in the upper mantle and 75–125 km in the lower mantle,
 379 which are comparable to the vertical grid interval. This is more than three times the resolution of
 380 the existing global tomography models ($>$ 500 km). The regions with a hit count $<$ 50 have low
 381 CRT recovery, which indicates that the regions not masked in white in the main tomographic
 382 results (Figures 5–8) have sufficient resolution.

383 In the output of RRTs (Figures 9b, 10a, and S18–S22), it can be seen that the pattern
384 recovery is lower in the vicinity of the MTZ beneath the Indian Ocean. In other regions, we can
385 see that the input patterns are generally recovered, although the input amplitudes tend to slightly
386 decrease. In the output of SRTs (Figures 9c–9i, 10b–10f, and S23–S57), the features of the input
387 models are reproduced very well, showing the robustness of the continuity of the Hainan plume
388 from the surface to CMB, and the features around the hole in the Australian slab.

389 **6. Discussion**

390 **6.1 Comparison with previous models**

391 First we give an overview of our model by comparing with the previous models focusing on
392 slab structures. Our novel Vp model clearly reveals subducted slabs as high-Vp bands at depths <
393 ~800 km with the resolution comparable to the previous regional tomography (Figures 5, 6, and
394 11). The bending of the subducting Indo-Australian slab beneath northern Sumatra (Hall &
395 Spakman, 2015; Pesicek et al., 2008) is confirmed at depths of 310–550 km (Figures 5, 11b, and
396 11c). However, our model shows another linear high-Vp band continuous from the south without
397 bending, suggesting another slab subducted from the intersecting trench (Figures 11b–11e). A
398 hole in the Australian slab beneath eastern Java, which was pointed out by many previous studies
399 (Hall & Spakman, 2015; Wehner et al., 2021; Widiyantoro et al., 2011; Zenonos et al., 2019), is
400 confirmed as a break in the high-Vp band at depths of 280–460 km, which is discussed in detail
401 in Section 6.5 (Figures 11a and 11b). The spoon-shaped Banda slab is also revealed at depths of
402 250–600 km, with a flat-lying portion at a depth of ~600 km (Hall & Spakman, 2015; Spakman
403 & Hall, 2010) (Figures 11a–11d). The Sangihe and Halmahera slabs beneath the Molucca Sea
404 (Hall & Spakman, 2015) are clearly separated by a linear low-Vp band sandwiched between the

405 high-Vp slabs at depths 250–800 km (Figure 11a and A-A' section in Figure 12). Vast high-Vp
406 anomalies in the MTZ due to the slab stagnation (Hua et al., 2022; Huang et al., 2015) are also
407 confirmed in our model (Figure 11d). In the lower mantle, a high-Vp body beneath Sunda
408 Shelf–Borneo–Philippines at depths of 900–1400 km (e.g., Hall & Spakman, 2015) is clearly
409 revealed in our model (Figures 6, 11g, and 11h).

410 Next we compare our model with the previous global tomography models. Ten P-wave
411 tomographic models are used for the comparison, i.e., UU-P07 (Amaru, 2007), MITP08 (Li et al.,
412 2008), GyPSuM-P (Simmons et al., 2010), LLNL_G3Dv3 (Simmons et al., 2012), GAP-P4
413 (Fukao & Obayashi, 2013; Obayashi et al., 2013), SPani-P (Tesoniero et al., 2015),
414 Hosseini2016 (Hosseini, 2016), MITP_USA_2016MAY (Burdick et al., 2017), TX2019slab-P
415 (Lu et al., 2019), and DETOX-P3 (Hosseini et al., 2020). These models were downloaded from
416 the SubMachine website (<http://www.earth.ox.ac.uk/~smachine/cgi/index.php>) (Hosseini et al.,
417 2018).

418 In Figures 13 and S58–S60 we compare these models with our model for four vertical cross-
419 sections. Our model is shown in the upper left, and all these models are displayed using the same
420 color scale. In Figure 13, passing through the Hainan hotspot, a low-Vp conduit elongated
421 vertically from the CMB toward the Earth's surface shows up clearly in our model, which may
422 be a hot mantle plume as pointed out by previous studies (e.g., Zhao et al., 2021). The Hainan
423 plume in the lower mantle is also visible in Hosseini2016 and DETOX-P3, but only our model
424 clearly shows the plume upwelling from the CMB. In other models, the low-Vp zone extends
425 over a wide area near the surface other than right beneath the Hainan area, and the characteristics
426 of the mantle plume are hard to see. In Figure S58 passing through Borneo and northern
427 Australia, the Australian slab subducting from the south can be traced to a depth of ~1400 km,

428 which is common to all models. On the other hand, only our model clearly images the low-Vp
429 anomaly corresponding to hot mantle upwelling in the mantle wedge beneath volcanic fronts. In
430 Figure S59 passing through Java, Borneo, and the Philippines, a U-shaped high-Vp zone that
431 combines the Australian and Philippine Sea slabs appears in all models except for GyPSuM-P
432 and SPani-P. However, in our model, the continuity between the U-shaped high-Vp zone and
433 deeper high-Vp anomalies can be seen more clearly. In Figure S60 passing through Sulawesi,
434 there are large discrepancies between models. Our model shows a high-Vp zone that might be
435 associated with slab remnants at depths $> \sim 1500$ km in the lower mantle, but similar features can
436 be seen only in DETOX-P3, Hosseini2016, LLNL_G3Dv3, MITP_USA_2016MAY, and
437 TX2019slab-P. Because TX2019slab-P is a model for which subducting slabs are introduced as a
438 priori information in the upper mantle, the similarity of the slab characteristics with this model
439 indicates the validity of our model.

440 **6.2 Comparison with plate reconstruction**

441 Assuming vertical slab subduction and mantle viscosity at a specific value, the depth of a
442 slab subducting from the trench is proportional to the subduction age. Therefore, a high-Vp
443 anomaly in the tomographic images can be associated with the corresponding slab subduction, by
444 comparing the tomography of a particular depth with the reconstructed plate position in a
445 particular age. The relationship between the subduction age and slab depth differs depending on
446 the study, but representative results by Lithgow-Bertelloni & Richards (1998) and Butterworth et
447 al. (2014) are shown in Figure S61. Using these relationships, the latest plate reconstruction by
448 Müller et al. (2019) is compared with the depth slices of our tomography. Figures 14 and S62
449 show the comparison using the age-depth relationship by Lithgow-Bertelloni & Richards (1998)
450 and Butterworth et al. (2014), respectively.

451 The most distinctive feature of these comparisons is coincidence of the vast high-Vp body
452 beneath Sunda Shelf–Borneo–Philippines at depths of 900–1400 km (e.g., Hall & Spakman,
453 2015) with the position of the “opposite subduction zone” where plates subduct from the two
454 subparallel trenches facing each other. For example, in Figure 14, the high-Vp body seems
455 located in a region sandwiched between two opposing trench axes at 33–75 Ma, and the area of
456 the high-Vp body decreases as the times go back and this region narrows. Before 90 Ma, the
457 opposite subduction zone collapses, and the high-Vp body synchronously disappears. Because
458 the horizontal movement of the subducted slabs may be small in the opposite subduction zone,
459 the assumption of vertical subduction seems to be reasonable. In Figure S62, location of the
460 high-Vp body shows good agreement with the opposite subduction at 69–100 Ma, but at 108 Ma,
461 the opposite subduction collapses and the high-Vp body disappears. Due to the difference in the
462 age-depth relationship, the correspondence of ages and trench locations vary between the two
463 comparisons. However, both comparisons commonly suggest that the high-Vp body is originated
464 from the slab subducted from the opposite subduction zone < 100 Ma.

465 Since the internal structure of the high-Vp body was not resolved in the conventional
466 tomography models, this body has been interpreted as a slab complex subducted from various
467 subduction zones (Hall & Spakman, 2015). However, in our tomography model, the central part
468 of high-Vp body at depths of 1150–1200 km is distributed in two lines (Figure 11h). This might
469 be because the shapes of the two slabs subducted from the opposite subduction zone are
470 relatively well preserved.

471 **6.3 The Hainan mantle plume**

472 Zhao et al. (2021) investigated the whole mantle structure beneath South China–Indochina–
473 SCS and revealed a mantle plume rising from the lower mantle beneath the Hainan hotspot and

474 the southeast Asia basalt province (SABP), although its low-Vp amplitude in the lower mantle
475 was weak and the root of the plume was unclear. For the first time, our tomographic images
476 clearly show that the mantle plume beneath these areas is continuous from the CMB to the
477 surface (A-A' to D-D' sections in [Figure 12](#)).

478 Looking to the south of these areas, a vast high-Vp body exists beneath the Sunda Shelf–
479 Borneo–Philippines at depths of 900–1400 km, which might be the deposition of subducted slabs
480 ([Section 6.2](#)). However, no apparent high-Vp anomaly is visible at depths of 1500–2200 km, and
481 the high-Vp zone becomes prominent again beneath Sulawesi–Philippines at depths $> \sim 2400$ km
482 (B-B' and b-b' to d-d' sections in [Figure 12](#)). This implies that the slabs subducted beneath this
483 area are polarized into those that have already fallen to the vicinity of the CMB and those that
484 remain shallower than 1400-km depth.

485 In the map view of our tomography at 2800 km depth ([Figure 6](#)), a high-Vp zone beneath
486 Sulawesi–Philippines is surrounded by low-Vp anomalies distributed beneath the SCS and Timor
487 Sea. Therefore, the hot mantle plume that formed the Hainan hotspot and SABP might be driven
488 by the downward mantle flow when the slabs currently lying on the CMB beneath Sulawesi–
489 Philippines subducted, but now its power has weakened because the slab portions has completely
490 fallen down to the CMB. A geochemical study pointed out that the ascending rate of the Hainan
491 mantle plume is very slow (< 1 cm/yr), and the supply of hot mantle materials is close to be
492 depleted ([Zou & Fan, 2010](#)), which is in good agreement with the inference from our
493 tomographic results.

494 **6.4 Subslab hot mantle upwelling (SHMU)**

495 Our tomography model shows that the Australian slab, imaged as a distinct high- V_p zone, is
496 penetrating into the lower mantle through the MTZ. Another notable feature is the existence of a
497 strong subslab low- V_p zone extending from the lower mantle toward the Indian Ocean and
498 Timor Sea (a-a' to d-d' sections in [Figure 15](#)). Hereafter we call the low- V_p zone “subslab hot
499 mantle upwelling (SHMU)”, which may be return flow generated as the slab subducts into the
500 lower mantle, and rises guided by the slab.

501 Recently, the importance of SHMU in the upper mantle that exists directly beneath the
502 subducting slab has begun to be recognized ([Fan & Zhao, 2021](#); [Wang et al., 2020](#)). For example,
503 [Fan & Zhao \(2021\)](#) obtained detailed tomographic images of the upper mantle in the world's six
504 subduction zones, and suggested a possibility that the occurrence of giant megathrust
505 earthquakes ($M > 8.5$) was affected by the upper-mantle SHMU because it may change the shape
506 of the slab due to its buoyancy. The SHMU revealed by this study seems more powerful
507 comparable to a hot mantle plume because it rises from the lower mantle and has large low- V_p
508 amplitudes. When such a powerful SHMU rises along the subducting slab and reaches beneath
509 the oceanic plate outside the trench axis, the oceanic plate might be thinned by thermal erosion
510 (a-a' section in [Figure 12](#)). As mentioned in [Section 1](#), SE Asia has grown by the separation of
511 continental slivers from the southern hemisphere and their movement to the northern hemisphere,
512 which might be driven by SHMU in addition to normal mantle convection.

513 **6.5 Slab hole beneath eastern Java**

514 Our model shows a hole in the Australian slab beneath eastern Java at depths of 280–460 km
515 ([Figure 15](#)). At depths of 310–400 km, low- V_p zones located inside and outside the subduction

516 zone seem connected through the slab hole, suggesting the existence of 3-D mantle flow as
517 pointed out by [Huang et al. \(2015\)](#). The reliability of these features is confirmed by seven SRTs
518 (SRT1–SRT7) ([Figures 9 and 10](#), also see [Section 5](#)). The existence of the slab hole is also
519 supported by the lack of slab seismicity there ([Hall & Spakman, 2015](#)).

520 In our tomography, bending of the slab can be confirmed near the bottom end of the slab hole
521 at a depth of 490 km ([Figure 15](#)). Because the slab hole is considered to have formed since ~8
522 Ma ([Hall & Spakman, 2015](#)), the age-depth relationship by [Lithgow-Bertelloni & Richards](#)
523 ([1998](#)) can be applicable. Comparison of the plate reconstruction by [Müller et al. \(2019\)](#) with our
524 tomography shows that the axis of the Sunda Trench disappears west of the slab bend at 10 Ma
525 ([Figure 14](#)). Therefore, we can infer that the slab hole was formed because the slab was partially
526 torn by a tectonic force such that shifts the trench axis at ~10 Ma. An alternative interpretation is
527 that the slab hole was formed by subduction of seamounts ([Hall & Spakman, 2015](#)). Further
528 research is needed regarding the origin of the slab hole.

529 There are two interesting features related to the slab hole. One is that the Tambora and
530 Rinjani volcanoes, which are the only two in this region of 25 world's volcanoes that caused
531 large volcanic eruptions during the past 2500 years ([Sigl et al., 2015](#)), are located just above the
532 east edge of this slab hole ([Figure 15](#)). The other feature is that the strong SHMU rising from the
533 lower mantle seems connected with the upper-mantle corner flow in the mantle wedge through
534 the slab hole ([Figure 16](#)). Considering these features together, we can infer that the catastrophic
535 volcanic eruptions specialized only in this area were driven by the supply of hot mantle materials
536 from the deep mantle comparable to a hot plume. A prominent K-rich feature of the Tambora
537 ignimbrites ([De Maisonneuve & Bergal-Kuvikas, 2019](#)) might support our interpretation, and
538 further support from geological and geochemical studies is needed.

539 **6.6 Structure of the D'' layer**

540 Our model shows a high-Vp band at depths of 2600–2800 km beneath from eastern Borneo
541 to the Philippine Sea Plate, whereas a low-Vp band located subparallel to the high-Vp band is
542 remarkable beneath the Timor Sea. Comparisons with plate reconstructions show that these
543 bodies are located just beneath an ancient subduction zone that existed at ~200 Ma (Figures 14
544 and S62). A recent study suggests that high-V zones in the lower mantle and the D'' layer (a 200-
545 300 km thick layer above the CMB) reflect the subducted slabs, whereas (at least parts of) the
546 low-V zones there may reflect the subducted oceanic crust materials (Jones et al., 2020).
547 Therefore, the low-Vp band beneath the Timor Sea might reflect the reworked oceanic crust,
548 where hot mantle upwelling could be born.

549 **7. Conclusions**

550 A detailed 3-D P-wave velocity (Vp) model of the whole mantle beneath SE Asia and
551 surrounding areas is obtained by inverting a large number of high-quality P-wave arrival-time
552 data recorded by seismic stations distributed all over the world. The 3-D Vp structure from the
553 lithosphere to the CMB is effectively resolved. The novel tomographic model reveals the
554 following new features.

555 (1) It has become clear for the first time that the hot mantle plume beneath the Hainan
556 hotspot is rising from the CMB. This hot plume may have been generated as a return flow as the
557 slab remnants beneath Sulawesi–Philippines fell down to the CMB. Currently, the Hainan mantle
558 plume seems to have weakened because the slab remnants had almost completely dropped down
559 to the CMB.

560 (2) A strong low- V_p anomaly is revealed beneath the Australian slab that has subducted into
561 the lower mantle. The low- V_p anomaly may reflect hot mantle upwelling due to return flow of
562 the slab subduction. We call it subslab hot mantle upwelling (SHMU). The SHMU confined to
563 the upper mantle has been found in many subduction zones in the world, but the one in this area
564 is unusual because it originates from the lower mantle and has large low- V_p amplitudes.

565 (3) The subducted slabs are revealed very clearly in both the upper and lower mantle. In
566 particular, a hole in the subducting Australian slab is clearly identified at depths of 280–460 km
567 beneath eastern Java. In and around the slab hole, 3-D mantle flow may exist. Corner flow in the
568 mantle wedge and the SHMU might be mixed through this slab hole, causing large-scale
569 volcanic eruptions in eastern Java.

570 **Acknowledgments**

571 We are grateful to Profs. Satoshi Miura and Toru Matsuzawa for helpful discussions.
572 Discussions with Ms. Masyitha Retno Budiati and Dr. Tomomi Okada motivated us to study SE
573 Asia. This work was partially supported by research grants from Japan Society for the Promotion
574 of Science (Nos. 18K03794, 19H01996 and 23224012). The GMT ([Wessel et al., 2013](#)) and
575 GPlates ([Müller et al., 2018](#)) software packages are used in this study. The arrival-time data are
576 downloaded from the ISC (<http://www.isc.ac.uk/>). Part of the event data are also downloaded
577 from the USGS (<https://www.usgs.gov/>). The SubMachine website
578 (<http://www.earth.ox.ac.uk/~smachine/cgi/index.php>) ([Hosseini et al., 2018](#)) was accessed to
579 generate vertical cross-sections of the global tomography models as shown in [Figure 13](#).
580 Archiving of data from this study is underway through Zenodo. Currently these data can be seen
581 in Supporting Information for review purposes.

582 **Author contributions**

583 Conceptualization: Genti Toyokuni, Dapeng Zhao

584 Data curation: Genti Toyokuni

585 Formal analysis: Genti Toyokuni, Kenkichi Kurata

586 Methodology: Dapeng Zhao, Genti Toyokuni

587 Resources: Genti Toyokuni, Dapeng Zhao

588 Visualization: Genti Toyokuni, Kenkichi Kurata

589 Writing – original draft: Genti Toyokuni, Dapeng Zhao

590 Writing – review & editing: Genti Toyokuni, Dapeng Zhao, Kenkichi Kurata

591 **References**

592 Amaru, M. L. (2007). Global travel time tomography with 3-D reference models. Ph. D. Thesis,
593 Utrecht University.

594 [http://dspace.library.uu.nl/bitstream/handle/1874/19338/index.htm;jsessionid=88B6AA4](http://dspace.library.uu.nl/bitstream/handle/1874/19338/index.htm;jsessionid=88B6AA4941C5E76FD65034D89D4065E0?sequence=17)
595 [941C5E76FD65034D89D4065E0?sequence=17](http://dspace.library.uu.nl/bitstream/handle/1874/19338/index.htm;jsessionid=88B6AA4941C5E76FD65034D89D4065E0?sequence=17)

596 Bird, P. (2003). An updated digital model of plate boundaries. *Geochemistry, Geophysics,*
597 *Geosystems*, 4(4), 1027. <https://doi.org/10.1029/2001GC000252>

598 Burdick, S., Vernon, F. L., Martynov, V., Eakins, J., Cox, T., Tytell, J., Mulder, T., White, M. C.,
599 Astiz, L., Pavlis, G. L., & van der Hilst, R. D. (2017). Model update May 2016: Upper-
600 mantle heterogeneity beneath North America from travel-time tomography with global
601 and USArray data. *Seismological Research Letters*, 88(2A), 319–325.

602 <https://doi.org/10.1785/0220160186>

- 603 Butterworth, N. P., Talsma, A. S., Müller, R. D., Seton, M., Bunge, H.-P., Schuberth, B. S. A.,
604 Shephard, G. E., & Heine, C. (2014). Geological, tomographic, kinematic and
605 geodynamic constraints on the dynamics of sinking slabs. *Journal of Geodynamics*, 73,
606 1–13. <https://doi.org/10.1016/j.jog.2013.10.006>
- 607 De Maisonneuve, C. B. & Bergal-Kuvikas, O. (2020). Timing, magnitude and geochemistry of
608 major Southeast Asian volcanic eruptions: identifying tephrochronologic markers.
609 *Journal of Quaternary Science*, 35, 272–287. <https://doi.org/10.1002/jqs.3181>
- 610 Fan, J., & Zhao, D. (2021). Subslab heterogeneity and giant megathrust earthquakes. *Nature*
611 *Geoscience*, 14, 349–353. <https://doi.org/10.1038/s41561-021-00728-x>
- 612 Filippova, A. I., & Solovey, O. A. (2021). Deep velocity structure of Southeast Asia from
613 Rayleigh wave group velocities: 3D isotropic model of the S-wave velocity distribution
614 in the upper mantle. *Geotectonics*, 55, 531–542.
615 <https://doi.org/10.1134/S0016852121040063>
- 616 Fukao, Y., & Obayashi, M. (2013). Subducted slabs stagnant above, penetrating through, and
617 trapped below the 660 km discontinuity. *Journal of Geophysical Research: Solid Earth*,
618 118, 5920–5938. <https://doi.org/10.1002/2013JB010466>
- 619 Hafkenschied, E., Buitert, S. J. H., Wortel, M. J. R., Spakman, W., & Bijwaard, H. (2001).
620 Modelling the seismic velocity structure beneath Indonesia: a comparison with
621 tomography. *Tectonophysics*, 333(1–2), 35–46. [https://doi.org/10.1016/S0040-
622 1951\(00\)00265-1](https://doi.org/10.1016/S0040-1951(00)00265-1)
- 623 Hall, R., & Spakman, W. (2015). Mantle structure and tectonic history of SE Asia.
624 *Tectonophysics*, 658, 14–45. <http://dx.doi.org/10.1016/j.tecto.2015.07.003>

- 625 Hosseini, K. (2016). Global multiple-frequency seismic tomography using teleseismic and core-
626 diffracted body waves. Ph. D. Thesis, Faculty of Geosciences, LMU München.
627 <https://doi.org/10.5282/edoc.19597>
- 628 Hosseini, K., Matthews, K. J., Sigloch, K., Shephard, G. E., Domeier, M., & Tsekhmistrenko, M.
629 (2018). SubMachine: Web-Based tools for exploring seismic tomography and other
630 models of Earth's deep interior. *Geochemistry, Geophysics, Geosystems*, 19(5), 1464-
631 1483. <https://doi.org/10.1029/2018GC007431>
- 632 Hosseini, K., Sigloch, K., Tsekhmistrenko, M., Zaheri, A., Nissen-Meyer, T., & Igel, H. (2020).
633 Global mantle structure from multifrequency tomography using *P*, *PP* and *P*-diffracted
634 waves. *Geophysical Journal International*, 220(1), 96–141.
635 <https://doi.org/10.1093/gji/ggz394>
- 636 Hua, Y., Zhao, D., & Xu, Y.-G. (2022). Azimuthal anisotropy tomography of the Southeast Asia
637 subduction system. *Journal of Geophysical Research: Solid Earth*, 127, e2021JB022854.
638 <https://doi.org/10.1029/2021JB022854>
- 639 Huang, J., & Zhao, D. (2004). Crustal heterogeneity and seismotectonics of the region around
640 Beijing, China. *Tectonophysics*, 385(1–4), 159–180.
641 <https://doi.org/10.1016/j.tecto.2004.04.024>
- 642 Huang, Z., Zhao, D., & Wang, L. (2015). P wave tomography and anisotropy beneath Southeast
643 Asia: Insight into mantle dynamics. *Journal of Geophysical Research: Solid Earth*, 120,
644 5154–5174. <https://doi.org/10.1002/2015JB012098>

- 645 Humphreys, E., & Clayton, R. W. (1988). Adaptation of back projection tomography to seismic
646 travel time problems. *Journal of Geophysical Research*, 93(B2), 1073–1085.
647 <https://doi.org/10.1029/JB093iB02p01073>
- 648 Jones, T. D., Maguire, R. R., van Keken, P. E., Ritsema, J., & Koelemeijer, P. (2020). Subducted
649 oceanic crust as the origin of seismically slow lower-mantle structures. *Progress in Earth
650 and Planetary Science*, 7, 17. <https://doi.org/10.1186/s40645-020-00327-1>
- 651 Jolivet, L., Faccenna, C., Becker, T., Tesauro, M., Sternai, P., & Bouilhol, P. (2018). Mantle
652 flow and deforming continents: From India-Asia convergence to Pacific subduction.
653 *Tectonics*, 37, 2887–2914. <https://doi.org/10.1029/2018TC005036>
- 654 Kennett, B. L. N., & Engdahl, E. R. (1991). Traveltimes for global earthquake location and phase
655 identification. *Geophysical Journal International*, 105, 429–465.
656 <https://doi.org/10.1111/j.1365-246X.1991.tb06724.x>
- 657 Lebedev, S., & Nolet, G. (2003). Upper mantle beneath Southeast Asia from S velocity
658 tomography. *Journal of Geophysical Research: Solid Earth*, 108(B1), 2048.
659 <https://doi.org/10.1029/2000JB000073>
- 660 Legendre, C. P., Zhao, L., & Chen, Q.-F. (2015). Upper-mantle shear-wave structure under East
661 and Southeast Asia from Automated Multimode Inversion of waveforms. *Geophysical
662 Journal International*, 203(1), 707–719. <https://doi.org/10.1093/gji/ggv322>
- 663 Li, C., & van der Hilst, R. D. (2010). Structure of the upper mantle and transition zone beneath
664 Southeast Asia from traveltome tomography. *Journal of Geophysical Research: Solid
665 Earth*, 115, B07308. <https://doi.org/10.1029/2009JB006882>

- 666 Li, C., van der Hilst, R. D., & Toksöz, M. N. (2006). Constraining P-wave velocity variations in
667 the upper mantle beneath Southeast Asia. *Physics of the Earth and Planetary Interiors*,
668 154(2), 180–195. <https://doi.org/10.1016/j.pepi.2005.09.008>
- 669 Li, C., van der Hilst, R. D., Engdahl, E. R., & Burdick, S. (2008). A new global model for P
670 wave speed variations in Earth's mantle. *Geochemistry Geophysics Geosystems*, 9(5),
671 Q05018. <https://doi.org/10.1029/2007GC001806>
- 672 Lithgow-Bertelloni, C., & Richards, M. A. (1998). The dynamics of Cenozoic and Mesozoic
673 plate motions. *Reviews of Geophysics*, 36(1), 27–78. <https://doi.org/10.1029/97RG02282>
- 674 Lu, C., Grand, S. P., Lai, H., & Garnero, E. J. (2019). TX2019slab: A new P and S tomography
675 model incorporating subducting slabs. *Journal of Geophysical Research: Solid Earth*,
676 124, 11549–11567. <https://doi.org/10.1029/2019JB017448>
- 677 Metcalfe, I. (2005). Asia: south-east. In: Selley, R. C., Cocks, L. R. M., Plimer, I. R. (Eds.),
678 *Encyclopedia of Geology*. Elsevier, Oxford, pp. 169–196.
679 <https://doi.org/10.1016/j.jseaes.2008.09.004>
- 680 Mishra, O. P., & Zhao, D. (2003). Crack density, saturation rate and porosity at the 2001 Bhuj,
681 India, earthquake hypocenter: A fluid driven earthquake? *Earth and Planetary Sciences*
682 *Letters*, 212(3–4), 393–405. [https://doi.org/10.1016/S0012-821X\(03\)00285-1](https://doi.org/10.1016/S0012-821X(03)00285-1)
- 683 Müller, R. D., Cannon, J., Qin, X., Watson, R. J., Gurnis, M., Williams, S., Pfaffelmoser, T.,
684 Seton, M., Russell, S. H. J., & Zahirovic, S. (2018). GPlates: Building a virtual Earth
685 through deep time. *Geochemistry, Geophysics, Geosystems*, 19, 2243–2261.
686 <https://doi.org/10.1029/2018GC007584>

- 687 Müller, R. D., Zahirovic, S., Williams, S. E., Cannon, J., Seton, M., Bower, D. J., Tetley, M. G.,
688 Heine, C., Le Breton, E., Liu, S., Russell, S. H. J., Yang, T., Leonard, J., & Gurnis, M.
689 (2019). A global plate model including lithospheric deformation along major rifts and
690 orogens since the Triassic. *Tectonics*, 38, 1884–1907.
691 <https://doi.org/10.1029/2018TC005462>
- 692 Obayashi, M., Yoshimitsu, J., Nolet, G., Fukao, Y., Shiobara, H., Sugioka, H., Miyamachi, H., &
693 Gao, Y. (2013). Finite frequency whole mantle P wave tomography: Improvement of
694 subducted slab images. *Geophysical Research Letters*, 40, 5652–5657.
695 <https://doi.org/10.1002/2013GL057401>
- 696 Paige, C. C., & Saunders, M. A. (1982). LSQR, An algorithm for sparse linear equations and
697 sparse least squares. *ACM Transactions on Mathematical Software (TOMS)*, 8(1), 43–71.
698 <https://doi.org/10.1145/355984.355989>
- 699 Pesicek, J. D., Thurber, C. H., Widiyantoro, S., Engdahl, E. R., & DeShon, H. R. (2008).
700 Complex slab subduction beneath northern Sumatra. *Geophysical Research Letters*, 35,
701 L20303. <https://doi.org/10.1029/2008GL035262>
- 702 Replumaz, A., Káráson, H., van der Hilst, R. D., Besse, J., & Tapponnier, P. (2004). 4-D
703 evolution of SE Asia's mantle from geological reconstructions and seismic tomography.
704 *Earth and Planetary Science Letters*, 221(1–4), 103–115. [https://doi.org/10.1016/S0012-](https://doi.org/10.1016/S0012-821X(04)00070-6)
705 [821X\(04\)00070-6](https://doi.org/10.1016/S0012-821X(04)00070-6)
- 706 Shi, H., Li, T., Zhang, R., Zhang, G., & Yang, H. (2020). Imaging of the upper mantle beneath
707 Southeast Asia: Constrained by teleseismic P-wave tomography, *Remote Sensing*, 12(18),
708 2975. <https://doi.org/10.3390/rs12182975>

- 709 Sigl, M., Winstrup, M., McConnell, J. R., Welten, K. C., Plunkett, G., Ludlow, F., Büntgen, U.,
710 Caffee, M., Chellman, N., Dahl-Jensen, D., Fischer, H., Kipfstuhl, S., Kostick, C.,
711 Maselli, O. J., Mekhaldi, F., Mulvaney, R., Muscheler, R., Pasteris, D. R., Pilcher, J. R.,
712 Salzer, M., Schüpbach, S., Steffensen, Vinther, B. M., & Woodruff, T. E. (2015). Timing
713 and climate forcing of volcanic eruptions for the past 2,500 years, *Nature*, 523, 54–5439.
714 <https://doi.org/10.1038/nature14565>
- 715 Simmons, N. A., Forte, A. M., Boschi, L., & Grand, S. P. (2010). GyPSuM: A joint tomographic
716 model of mantle density and seismic wave speeds. *Journal of Geophysical Research:*
717 *Solid Earth*, 115, B12310. <https://doi.org/10.1029/2010JB007631>
- 718 Simmons, N. A., Myers, S. C., Johannesson, G., & Matzel, E. (2012). LLNL-G3Dv3: Global P
719 wave tomography model for improved regional and teleseismic travel time prediction.
720 *Journal of Geophysical Research: Solid Earth*, 117, B10302.
721 <https://doi.org/10.1029/2012JB009525>
- 722 Spakman, W., & Hall, R. (2010). Surface deformation and slab–mantle interaction during Banda
723 arc subduction rollback. *Nature Geoscience*, 3, 562–566. <https://doi.org/10.1038/ngeo917>
- 724 Tesoniero, A., Auer, L., Boschi, L., & Cammarano, F. (2015). Hydration of marginal basins and
725 compositional variations within the continental lithospheric mantle inferred from a new
726 global model of shear and compressional velocity. *Journal of Geophysical Research:*
727 *Solid Earth*, 120, 7789–7813. <https://doi.org/10.1002/2015JB012026>
- 728 Toyokuni, G., Matsuno, T., & Zhao, D. (2020). *P* wave tomography beneath Greenland and
729 surrounding regions: 2. Lower mantle. *Journal of Geophysical Research: Solid Earth*,
730 125, e2020JB019839. <https://doi.org/10.1029/2020JB0198379>

- 731 Toyokuni, G., Zhao, D., & Chen, K. H. (2021). Structural control on the 2018 and 2019 Hualien
732 earthquakes in Taiwan. *Physics of the Earth and Planetary Interiors*, 312, 106673.
733 <https://doi.org/10.1016/j.pepi.2021.106673>
- 734 Um, J., & Thurber, C. (1987). A fast algorithm for two-point seismic ray tracing. *Bulletin of the*
735 *Seismological Society of America*, 77(3), 972–986.
- 736 Wang, X., Chen, Q.-F., Niu, F., Wei, S., Ning, J., Li, J., Wang, W., Buchen, J., & Liu, L. (2020).
737 Distinct slab interfaces imaged within the mantle transition zone. *Nature Geoscience*, 13,
738 822–827. <https://doi.org/10.1038/s41561-020-00653-5>
- 739 Wehner, D., Blom, N., Rawlinson, N., Daryono, D., Boehm, C., Miller, M. S., Supendi, P., &
740 Widiyantoro, S. (2021). SASSY21: A 3-D seismic structural model of the lithosphere and
741 underlying mantle beneath Southeast Asia from multi-scale adjoint waveform
742 tomography. <https://doi.org/10.1002/essoar.10507767.1>
- 743 Wei, W., Xu, J., Zhao, D., & Shi, Y. (2012). East Asia mantle tomography: New insight into
744 plate subduction and intraplate volcanism. *Journal of Asian Earth Sciences*, 60, 88–103.
745 <https://doi.org/10.1016/j.jseaes.2012.08.001>
- 746 Wessel, P., Smith, W. H. F., Scharroo, R., Luis, J., & Wobbe, F. (2013). Generic Mapping Tools:
747 Improved Version Released. *Eos, Transactions, American Geophysical Union*, 94(45),
748 409. <https://doi.org/10.1002/2013EO450001>
- 749 Widiyantoro, S., Pesicek, J. D., & Thurber, C. H. (2011). Subducting slab structure below the
750 eastern Sunda arc inferred from non-linear seismic tomographic imaging. *Geological*
751 *Society, London, Special Publications*, 355, 139–155. <https://doi.org/10.1144/SP355.7>

- 752 Yang, T., Gurnis, M., & Zahirovic, S. (2016). Mantle-induced subsidence and compression in SE
753 Asia since the early Miocene. *Geophysical Research Letters*, 43, 1901–1909.
754 <https://doi.org/10.1002/2016GL068050>
- 755 Yang, Z., Zhao, D., Dong, Y., & Cheng, B. (2022). Crustal flow and fluids affected the 2021
756 M7.4 Maduo earthquake in Northeast Tibet. *Journal of Asian Earth Sciences*, 225,
757 105050. <https://doi.org/10.1016/j.jseaes.2021.105050>
- 758 Zahirovic, S., Flament, N., Müller, R. D., Seton, M., & Gurnis, M. (2016). Large fluctuations of
759 shallow seas in low-lying Southeast Asia driven by mantle flow. *Geochemistry,*
760 *Geophysics, Geosystems*, 17, 3589–3607. <http://dx.doi.org/10.1002/2016GC006434>
- 761 Zenonos, A., De Siena, L., Widiyantoro, S., & Rawlinson, N. (2019). P and S wave travel time
762 tomography of the SE Asia-Australia collision zone. *Physics of the Earth and Planetary*
763 *Interiors*, 293, 106267. <https://doi.org/10.1016/j.pepi.2019.05.010>
- 764 Zhao, D. (2015). *Multiscale Seismic Tomography*, 304 pp. Tokyo: Springer.
765 <https://doi.org/10.1007/978-4-431-55360-1>
- 766 Zhao, D. (2004). Global tomographic images of mantle plumes and subducting slabs: insight into
767 deep Earth dynamics. *Physics of the Earth and Planetary Interiors*, 146, 3–34.
768 <https://doi.org/10.1016/j.pepi.2003.07.032>
- 769 Zhao, D., Fujisawa, M., & Toyokuni, G. (2017). Tomography of the subducting Pacific slab and
770 the 2015 Bonin deepest earthquake (Mw 7.9). *Scientific Reports*, 7, 44487.
771 <https://doi.org/10.1038/srep44487>

772 Zhao, D., Hasegawa, A., & Horiuchi, S. (1992). Tomographic imaging of P and S wave velocity
773 structure beneath northeastern Japan. *Journal of Geophysical Research*, 97, 19909–
774 19928. <https://doi.org/10.1029/92JB00603>

775 Zhao, D., Toyokuni, G., & Kurata, K. (2021). Deep mantle structure and origin of Cenozoic
776 intraplate volcanoes in Indochina, Hainan and South China Sea. *Geophysical Journal
777 International*, 225, 572–588. <https://doi.org/10.1093/gji/ggaa605>

778 Zhao, D., Yamamoto, Y., & Yanada, T. (2013). Global mantle heterogeneity and its influence on
779 teleseismic regional tomography. *Gondwana Research*, 23, 595–616.
780 <https://doi.org/10.1016/j.gr.2012.08.004>

781 Zou, H., & Fan, Q. (2010). U-Th isotopes in Hainan basalts: implications for sub-asthenospheric
782 origin of EM2 mantle endmember and the dynamics of melting beneath Hainan Island.
783 *Lithos*, 116, 145–152. <https://doi.org/10.1016/j.lithos.2010.01.010>

784

785

786

787

788

789

790

791

792

793

794

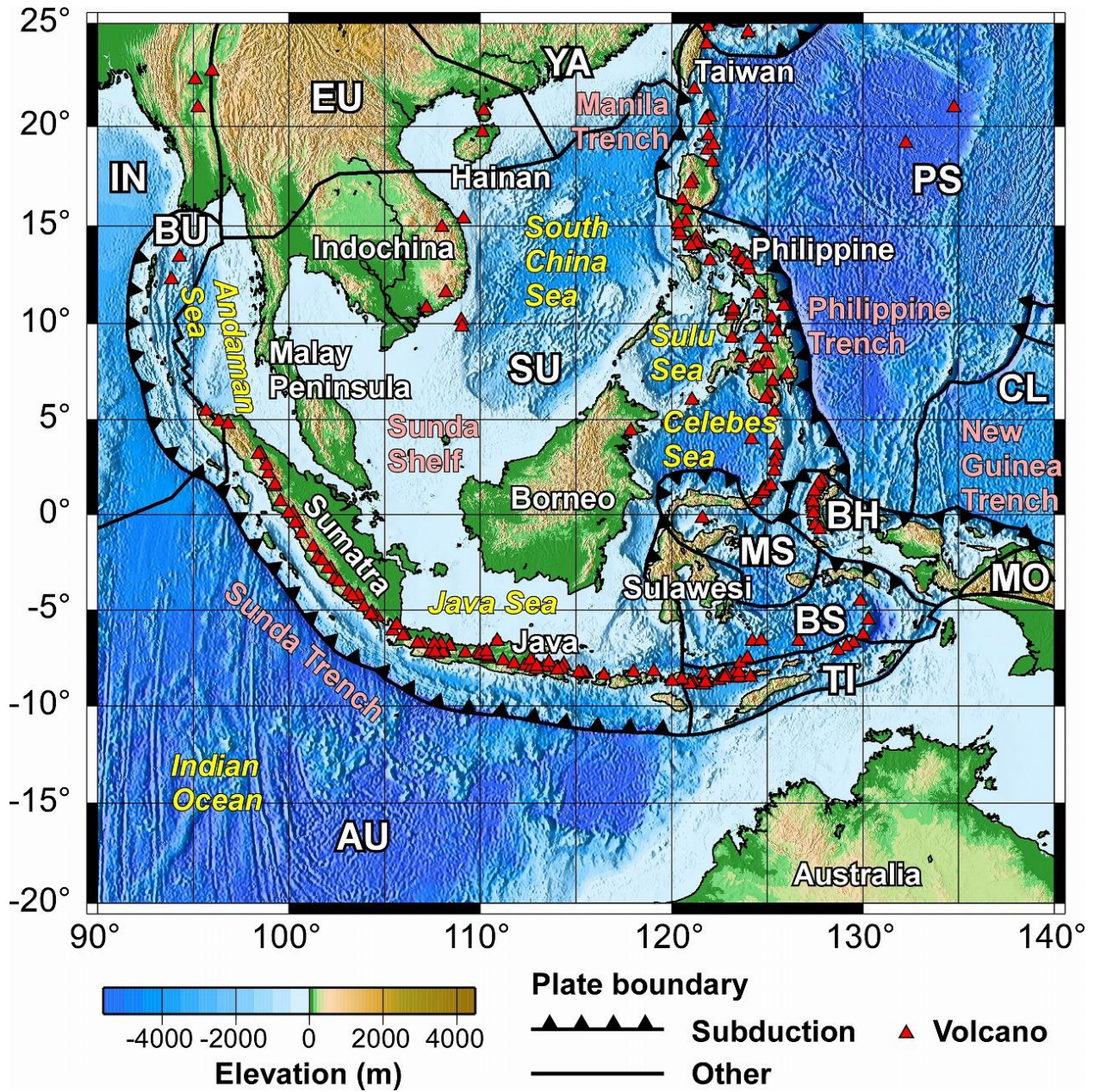
795 **Table 1.** Information on the 10 resolution tests performed by this study.

| Name | Description of the initial model |
|------|---|
| CRT1 | Checkerboard resolution test #1. Lateral grid interval is 278 km (a great circle distance of 2.5° on the surface) inside the study region, and 556 km (a great circle distance of 5° on the surface) in other regions (Table S2). |
| CRT2 | Checkerboard resolution test #2. Lateral grid interval is 167 km (a great circle distance of 1.5° on the surface) inside the study region, and 334 km (a great circle distance of 3° on the surface) in other regions (Table S3). |
| RRT | Restoring resolution test. Highlights the pattern of actual tomographic results, containing high-V (+1.5%) and low-V (−1.5%). |
| SRT1 | <p>Synthetic resolution test #1. Input model contains the following structures:</p> <ol style="list-style-type: none"> (1) Subducting Australian slab with high-V (+1.5%) at depths of 15–725 km. (2) Hot mantle upwelling in the mantle wedge with low-V (−1.5%) at depths of 15–500 km. (3) Subslab hot mantle upwelling (SHMU) with low-V (−1.5%) at depths of 150–1500 km. (4) A hole in the Australian slab between depths 260–460 km and latitudes 110°–115° with no velocity perturbation. (5) A low-V (−1.5%) bridge elongated in the latitudinal direction with the width of 2° in the longitudinal direction between depths 260–460 km, connecting (2) and (3) through the slab hole (4). (6) A low-V (−1.5%) conduits with a radius of 222 km (a great circle distance of 2° on the surface) elongated between depths 15–2800 km beneath the Hainan hotspot. |
| SRT2 | Synthetic resolution test #2. Input model is same as SRT1 but without (5). |
| SRT3 | Synthetic resolution test #3. Input model is same as SRT1 but without (4) and (5). |
| SRT4 | Synthetic resolution test #4. Input model is same as SRT1 but without (3) and (5). |
| SRT5 | Synthetic resolution test #5. Input model is same as SRT1 but without (2) and (5). |
| SRT6 | Synthetic resolution test #6. Input model is same as SRT1 but without (2), (3), and (5). |
| SRT7 | Synthetic resolution test #7. Input model is same as SRT1 but without (2), (3), (4), and (5). |

796

797

798



804 Caroline Plate; EU = Eurasian Plate; IN = Indian Plate; MO = Maoke Plate; MS = Molucca Sea
805 Plate; PS = Philippine Sea Plate; SU = Sunda Plate; TI = Timor Plate; YA = Yangtze Plate.

806

807

808

809

810

811

812

813

814

815

816

817

818

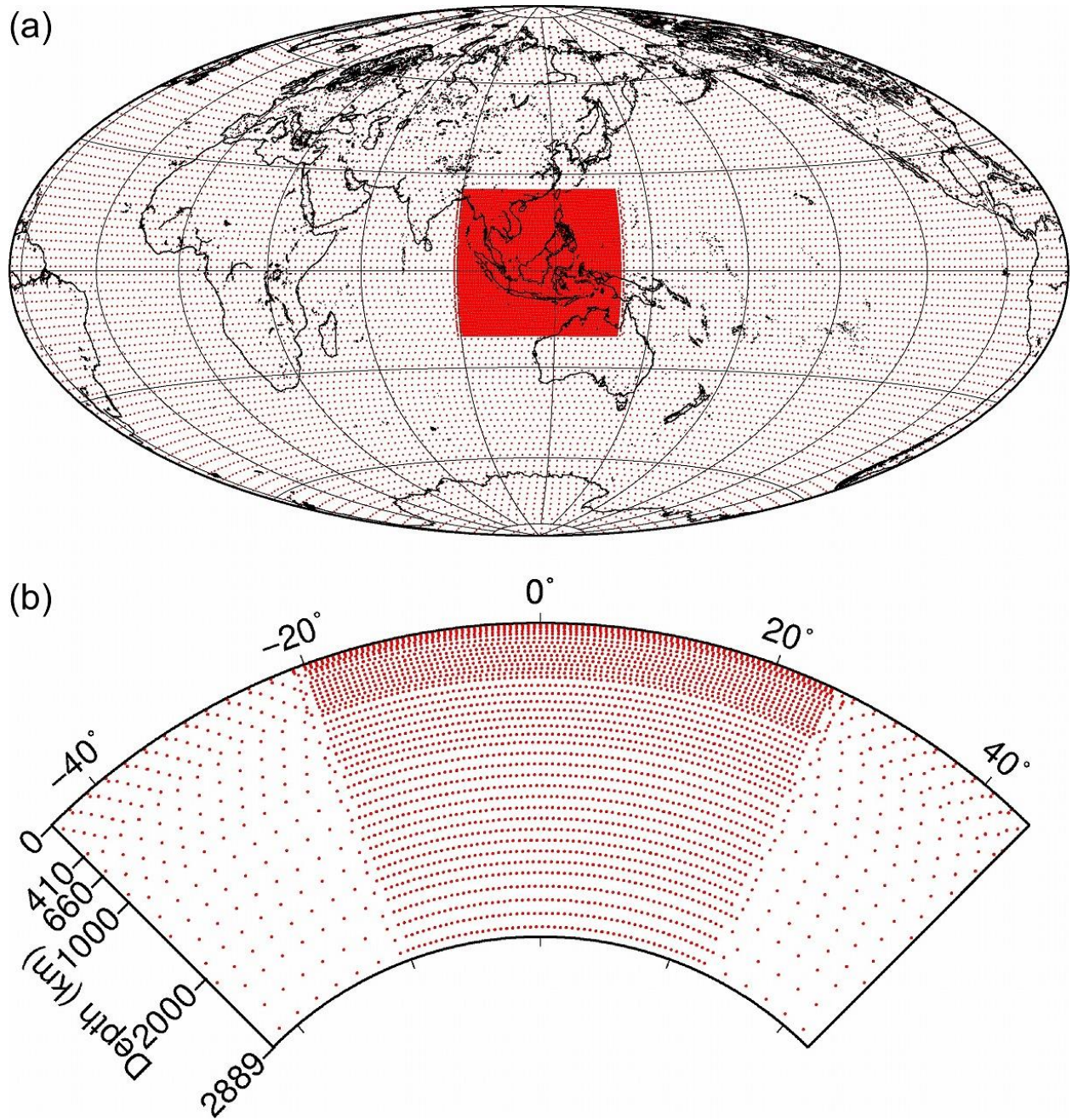
819

820

821

822

823



824

825

826 **Figure 2.** (a) Map view at a depth of 15 km and (b) N-S vertical cross-section along the
827 longitude of 115° showing the 3-D grid nodes adopted for the tomographic inversion. In the

828 target area (the red box in (a)), a denser grid is arranged, whereas a coarser grid is set up in the
829 surrounding crust and mantle of the Earth. The numbers atop (b) denote latitudes.

830

831

832

833

834

835

836

837

838

839

840

841

842

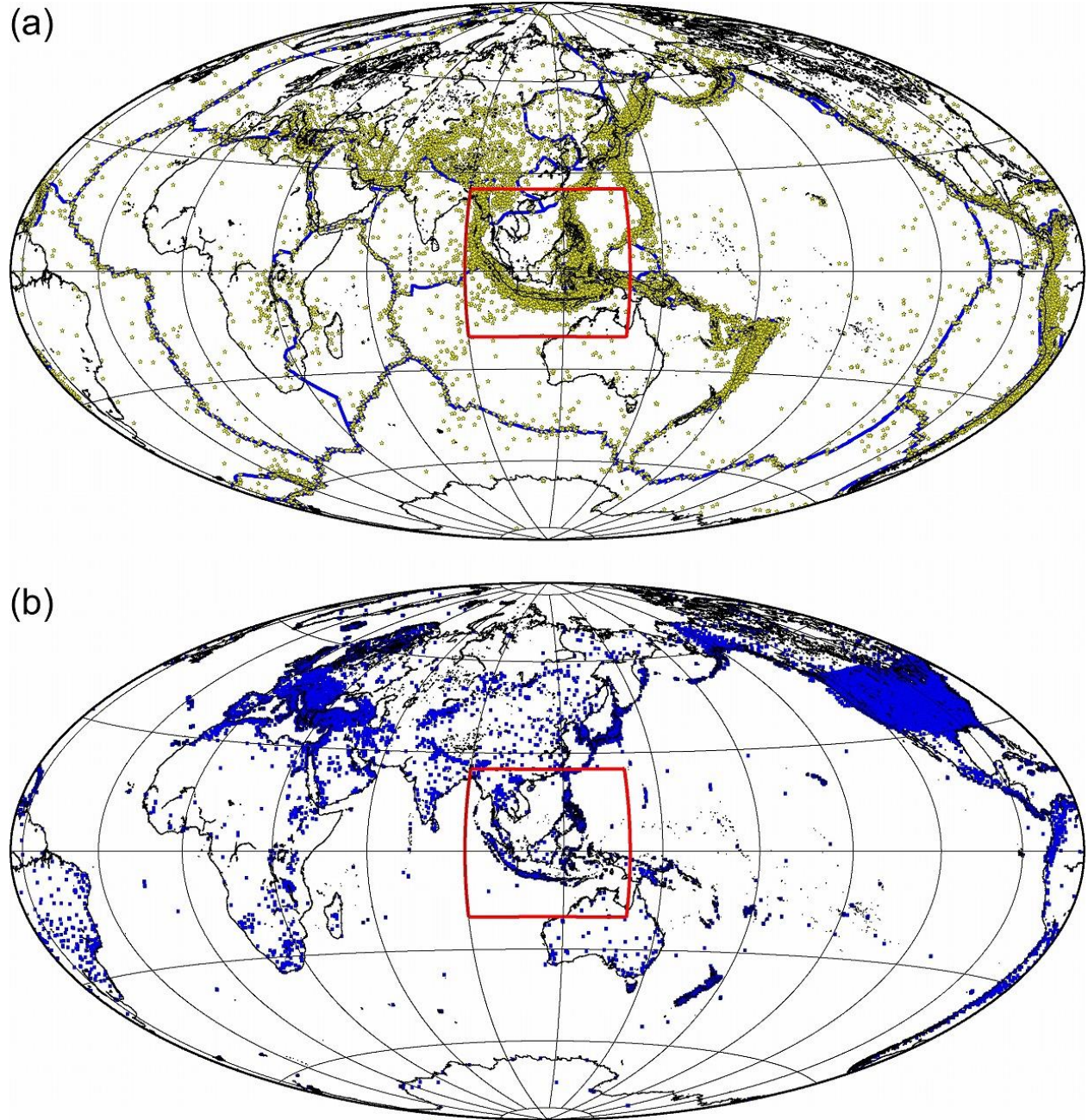
843

844

845

846

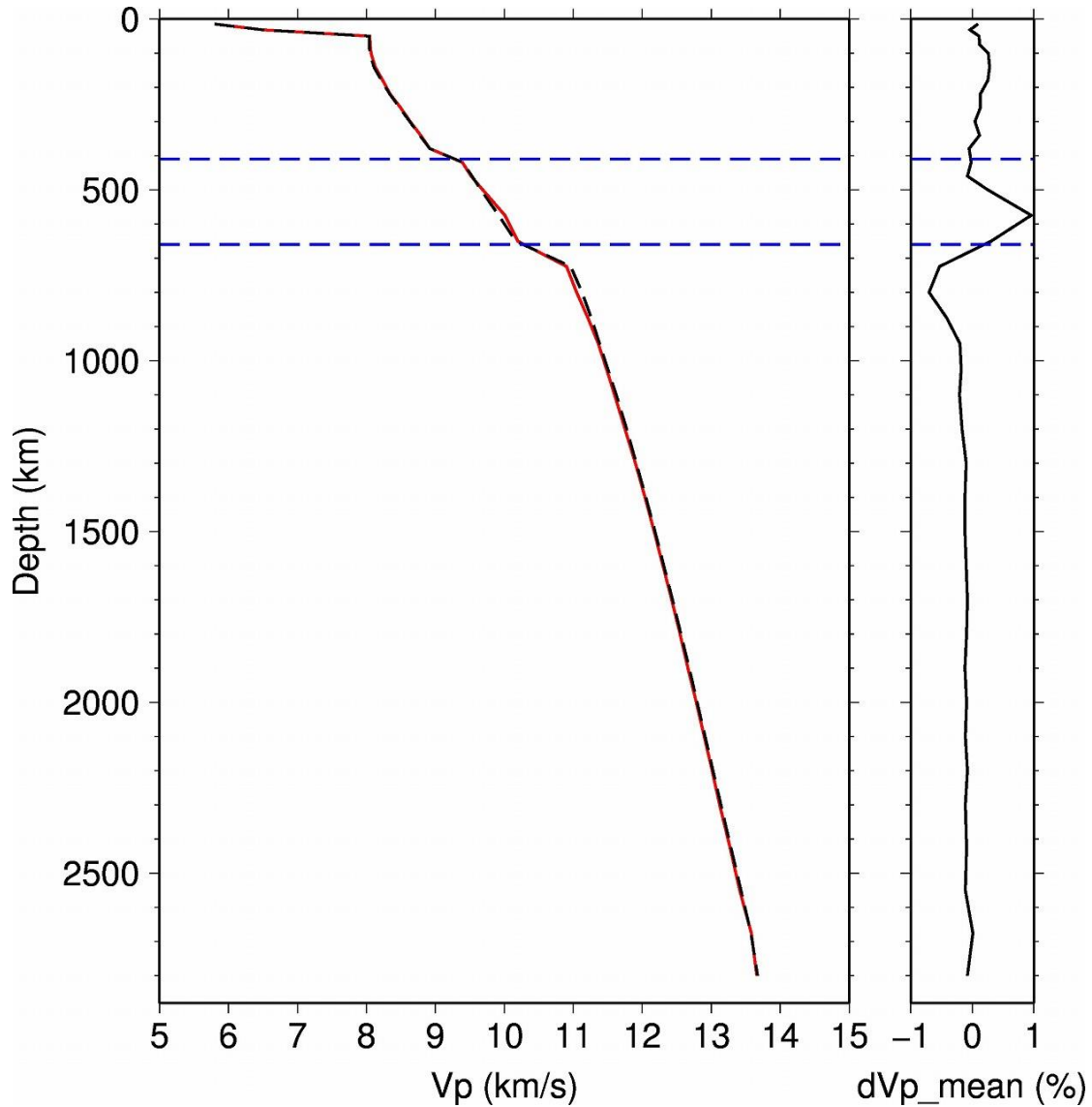
847



848

849 **Figure 3.** Distribution of 23,587 earthquakes **(a)** and 14,136 seismic stations **(b)** used in the
850 tomographic inversion. The red box indicates the target area. The thick black lines denote plate
851 boundaries.

852



853

854 **Figure 4. (Left)** The starting 1-D P-wave velocity model (IASP91, [Kennett & Engdahl, 1991](#))

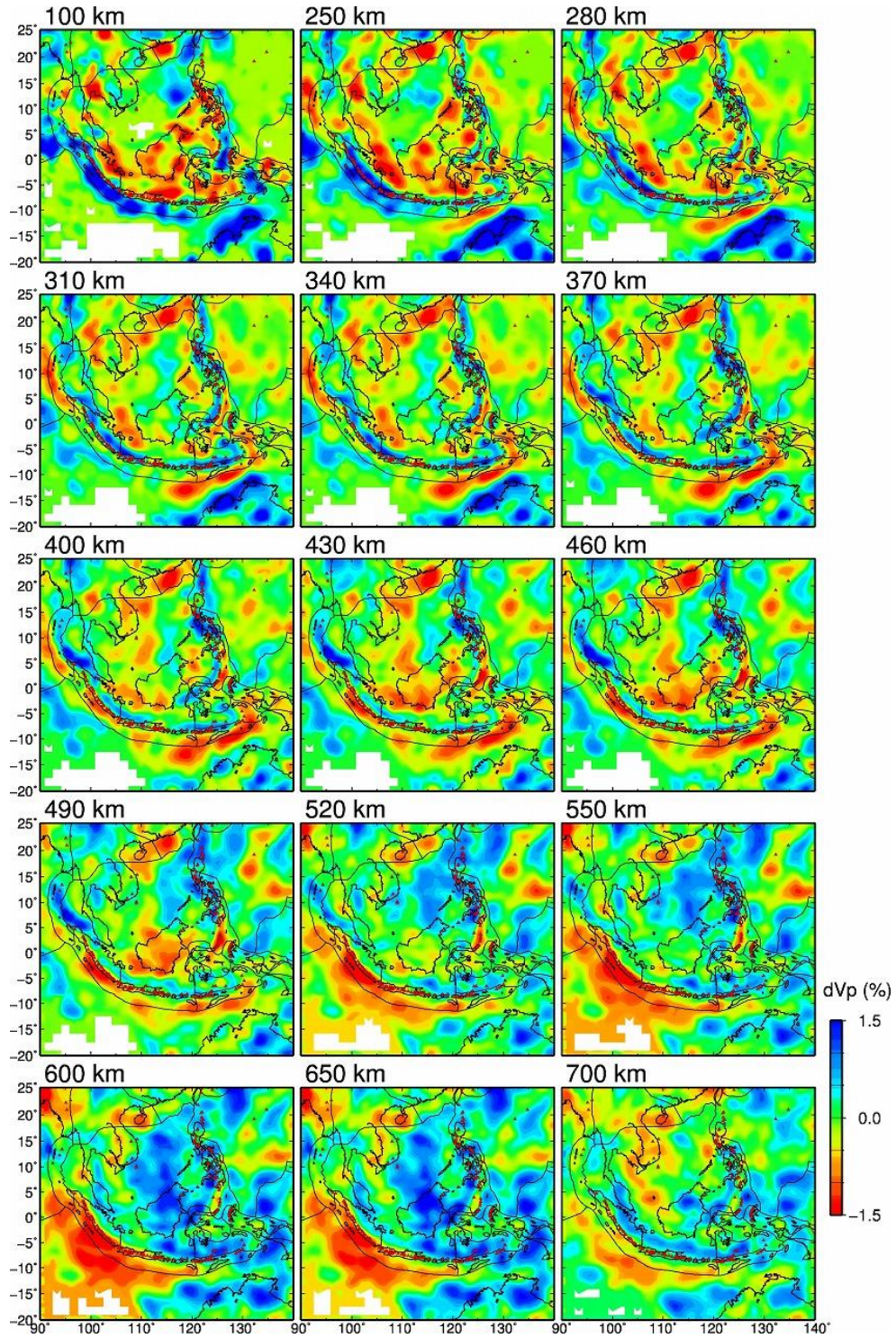
855 adopted for the tomographic inversions (black dotted line), and optimized 1-D P-wave velocity

856 model after subtracting the average velocity anomaly of the tomographic results at each depth

857 (red solid line). **(Right)** Depth distribution of the average velocity anomaly. The blue dotted lines

858 denote 410 and 660 km indicating the range of the mantle transition zone.

859



860

861 **Figure 5.** Map views of V_p tomography at depths of 100–700 km obtained by this study. The

862 layer depth is shown at the upper-right corner of each map. The blue and red colors denote high

863 and low V_p perturbations, respectively, whose scale (in %) is shown on the right. Areas with hit
864 counts < 50 are masked in white. The red triangles and thick black lines denote the active
865 volcanoes and plate boundaries, respectively.

866

867

868

869

870

871

872

873

874

875

876

877

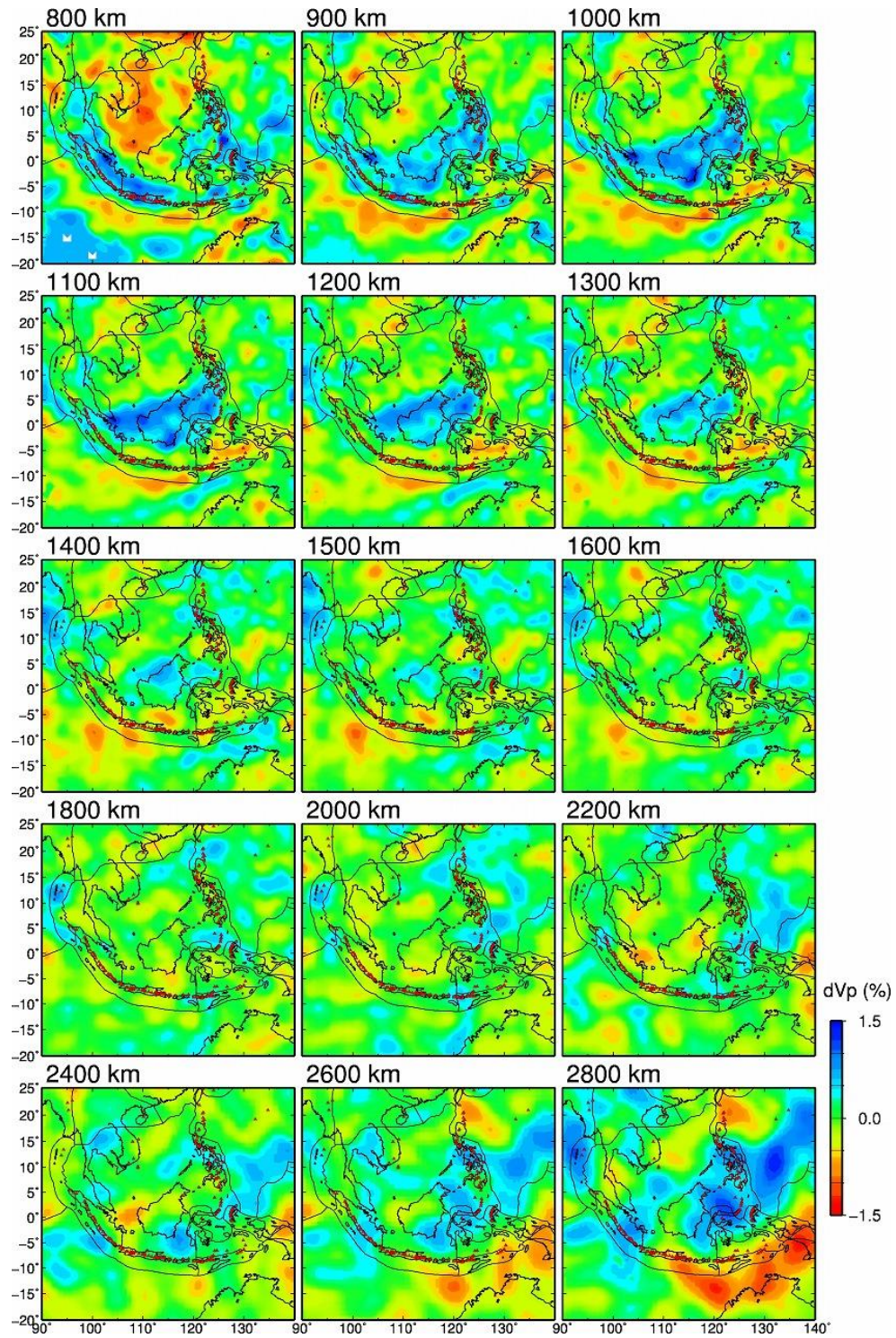
878

879

880

881

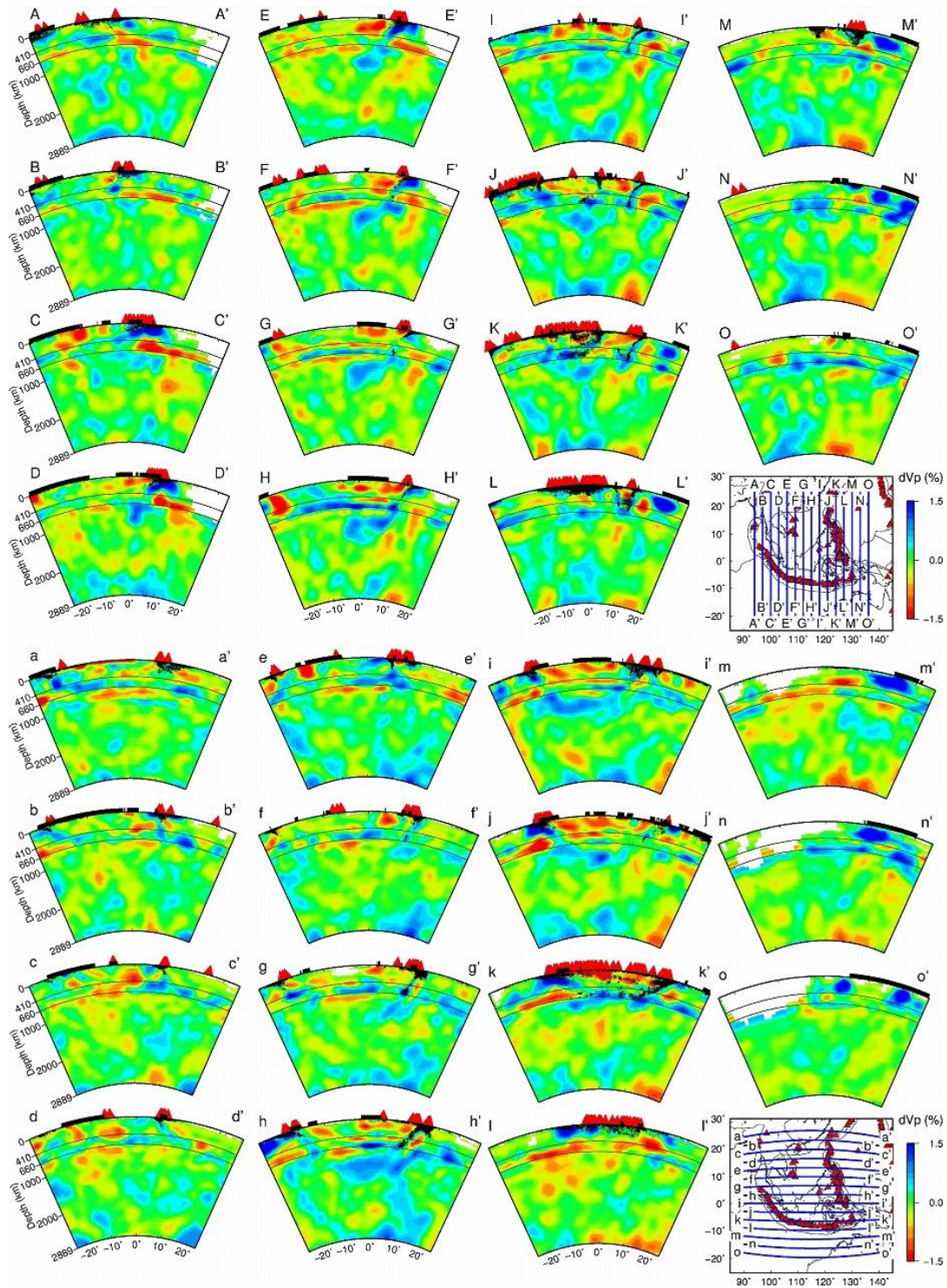
882



883

884 **Figure 6.** Same as [Figure 5](#) but for V_p images at depths of 800–2800 km.

885



886

887 **Figure 7.** Vertical cross-sections of Vp tomography along **(top)** 15 profiles in the N-S direction

888 (A-A' to O-O'), and **(bottom)** 15 profiles in the E-W direction (a-a' to o-o') as shown on the

889 inset map. The 410-km and 660-km discontinuities are shown in black solid lines. The thick
890 black lines on the surface denote land areas. Other labels are the same as those in [Figure 5](#).

891

892

893

894

895

896

897

898

899

900

901

902

903

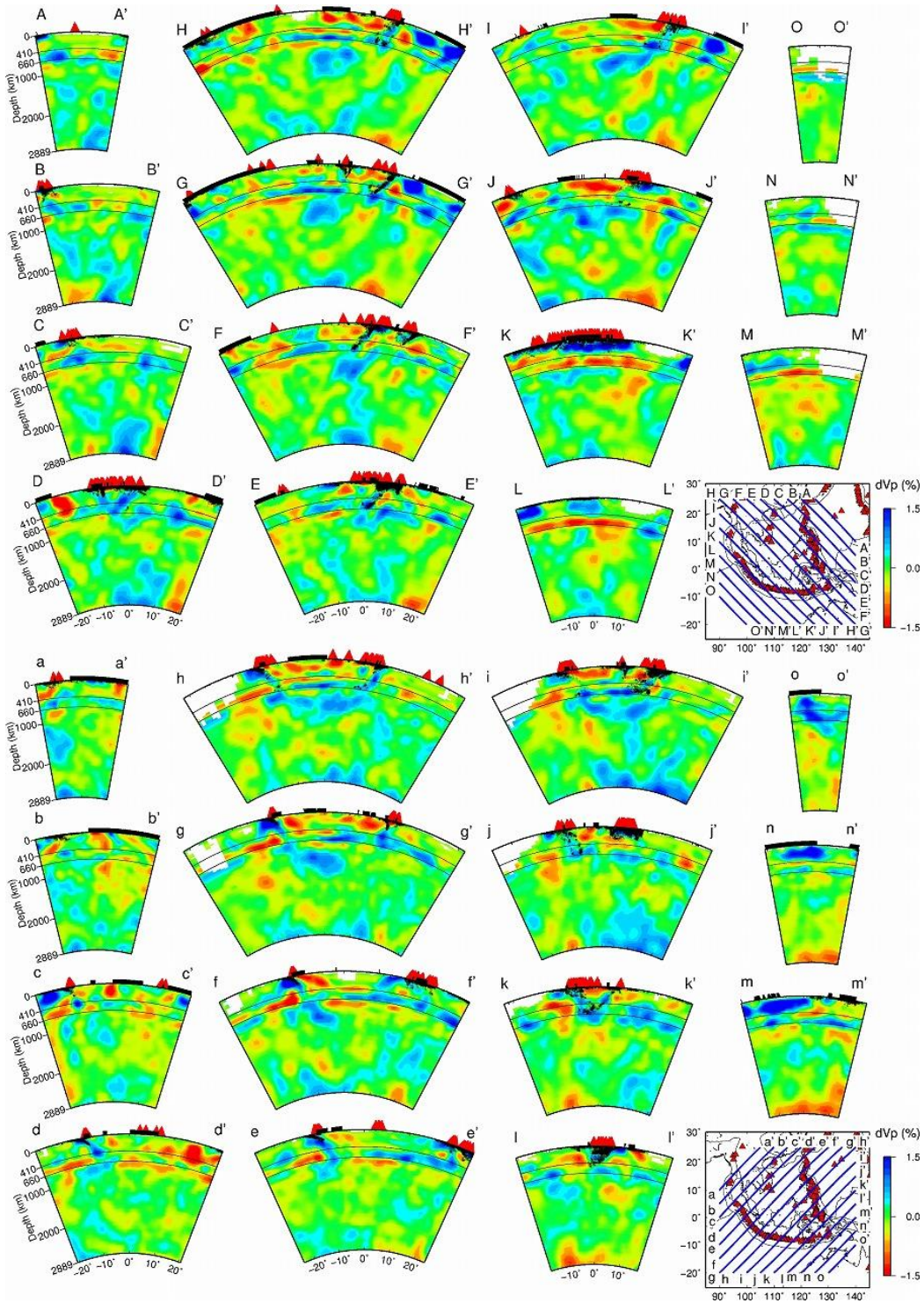
904

905

906

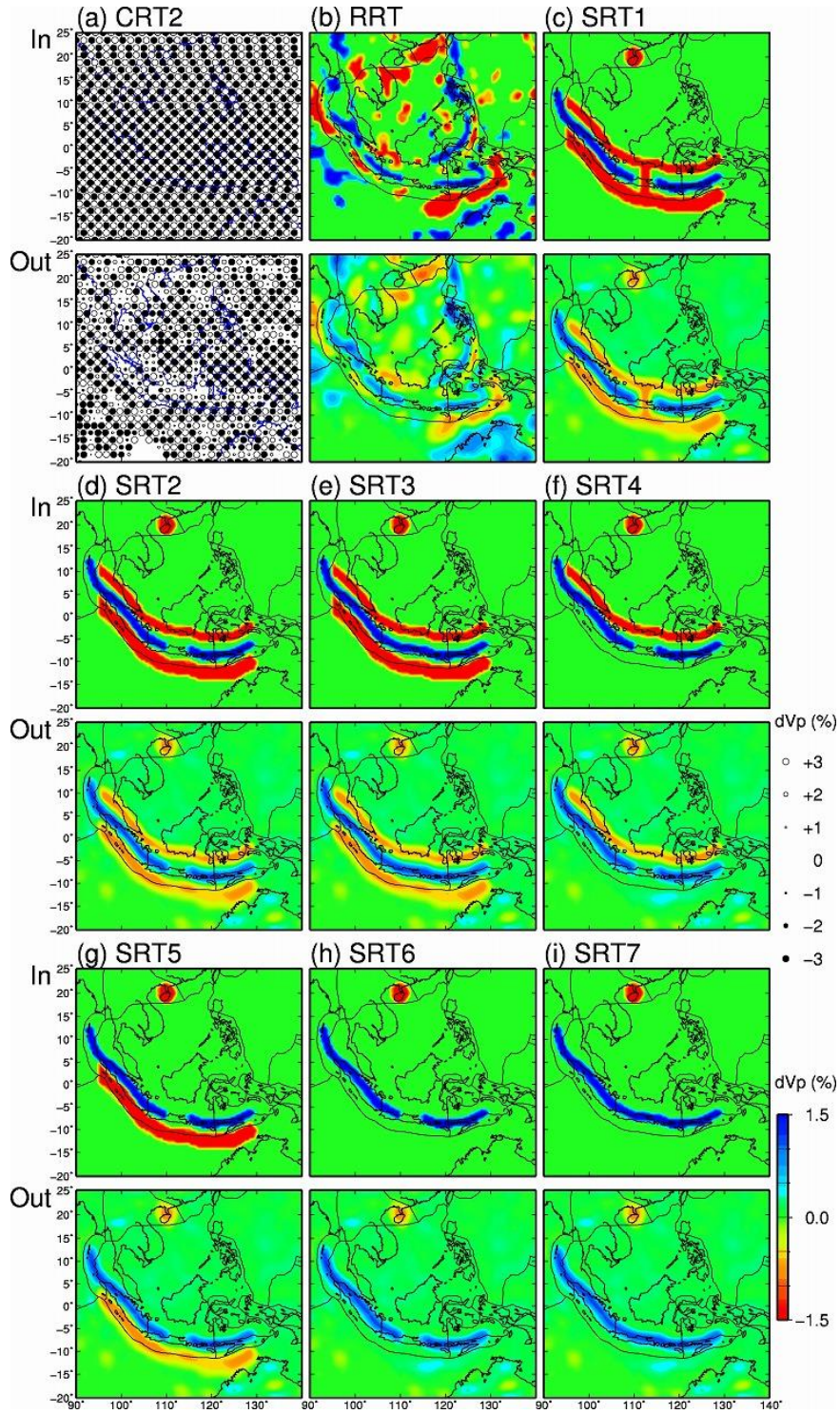
907

908



909 **Figure 8.** The same as [Figure 7](#) but along (top) 15 profiles in the NW-SE direction (A-A' to O-
 910 O'), and (bottom) 15 profiles in the NE-SW direction (a-a' to o-o').

911



912

913 **Figure 9.** Summary of the resolution tests. Map view images at a depth of 380 km of the (a)

914 CRT2, (b) RRT, (c) SRT1, (d) SRT2, (e) SRT3, (f) SRT4, (g) SRT5, (h) SRT6, and (i) SRT7.

915 The input (upper panel) and output (lower panel) models are shown for each test. The V_p
916 perturbation scales (in %) are shown on the right.

917

918

919

920

921

922

923

924

925

926

927

928

929

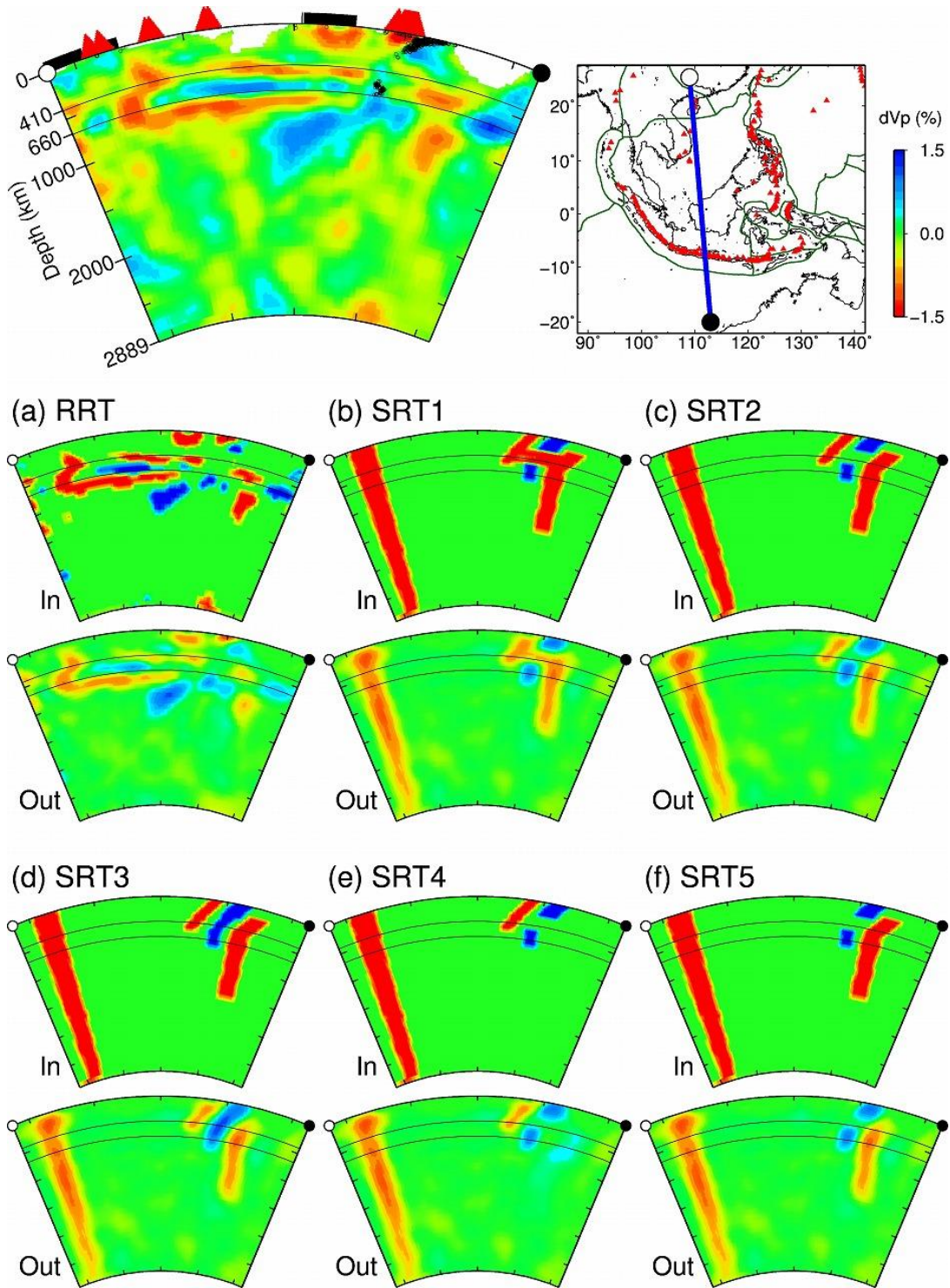
930

931

932

933

934



935

936 **Figure 10.** Summary of the resolution tests and comparison with the obtained real tomographic
 937 result (the upper-left panel). Vertical cross-sections through a hole in the Australian slab and the

938 Hainan hotspot for **(top)** actual tomography, **(a)** RRT, **(b)** SRT1, **(c)** SRT2, **(d)** SRT3, **(e)** SRT4,
939 and **(f)** SRT5. The input (upper panel) and output (lower panel) models are shown for each test.
940 The location of the cross-section and the Vp perturbation scale (in %) are shown at the top right.
941 Other labels are the same as those in [Figure 7](#).

942

943

944

945

946

947

948

949

950

951

952

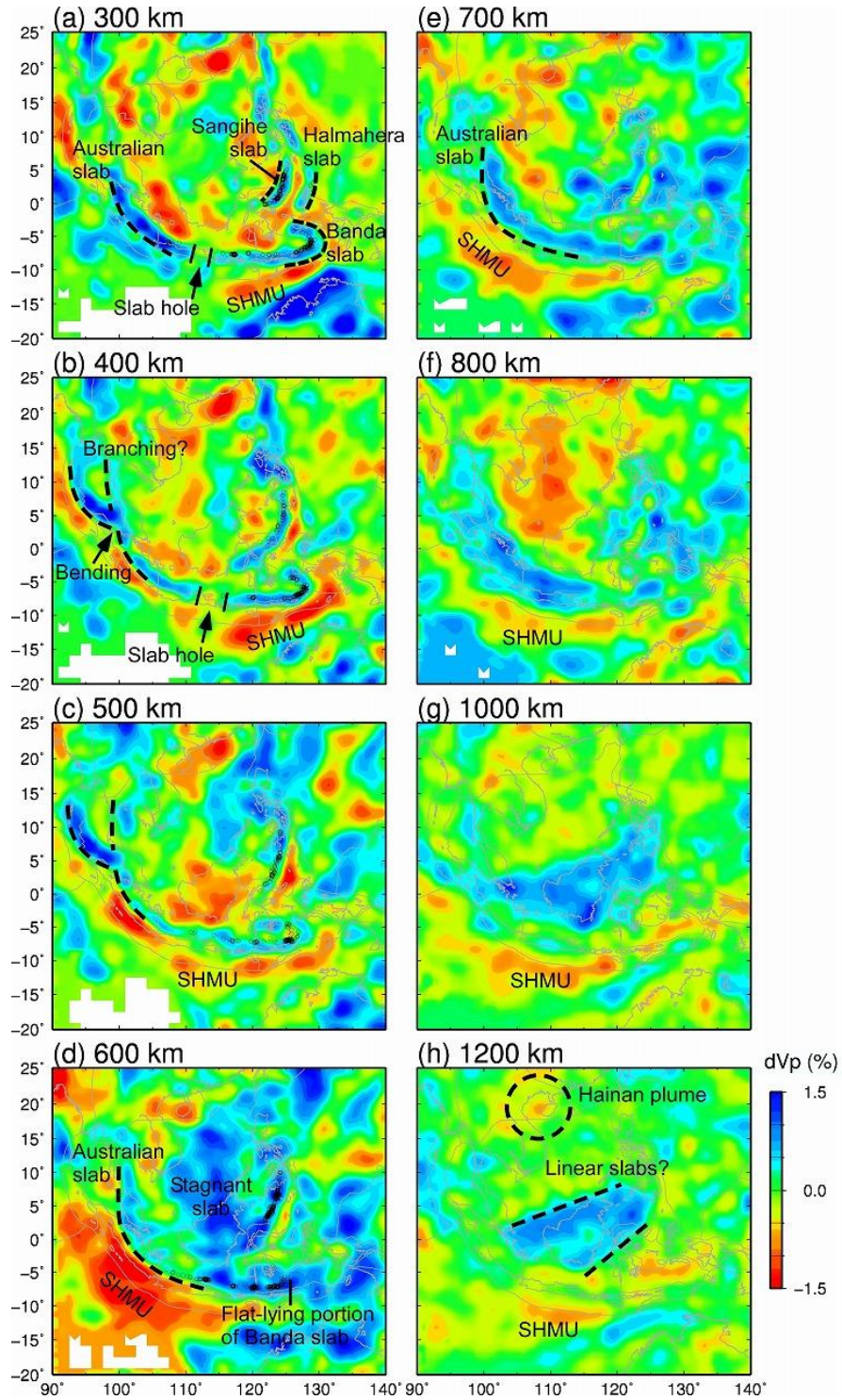
953

954

955

956

957



958

959 **Figure 11.** Summary and interpretation of Vp map views at depths of 300–1200 km. The Vp
 960 perturbation scale (in %) is shown on the right. The coastline and plate boundaries are shown in

961 gray to make the velocity images easier to see. The open circles denote local seismicity within a
962 ± 30 -km depth range of each layer. SHMU = slab hot mantle upwelling.

963

964

965

966

967

968

969

970

971

972

973

974

975

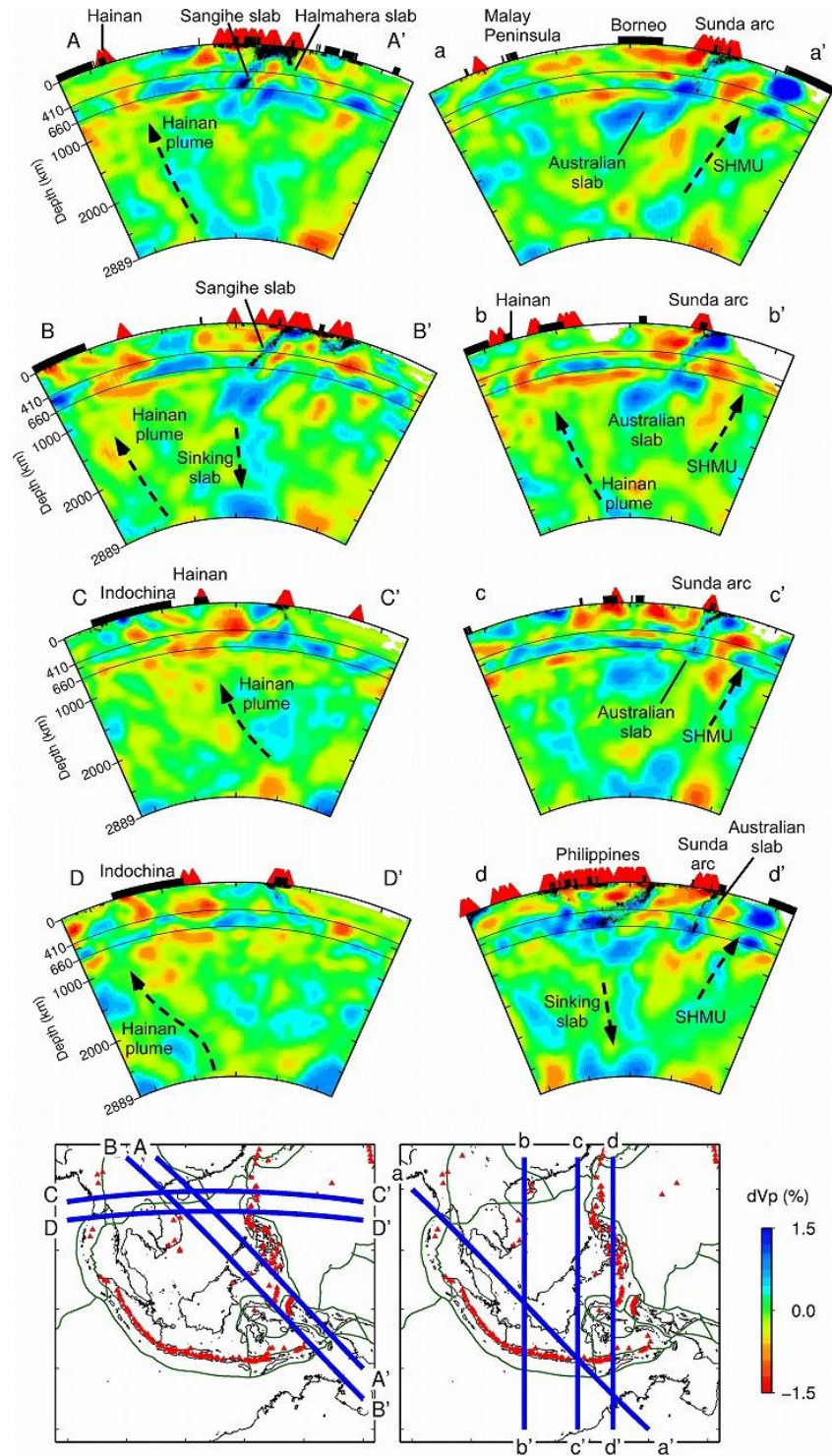
976

977

978

979

980



981

982 **Figure 12.** Summary and interpretation of V_p vertical cross-sections through (left) the Hainan

983 hotspot and Indochina (A-A' to D-D'), and (right) the Australian slab (a-a' to d-d'), whose

984 locations are shown on the inset maps at the bottom. The V_p perturbation scale (in %) is shown
985 on the right. Other labels are the same as those in [Figure 7](#).

986

987

988

989

990

991

992

993

994

995

996

997

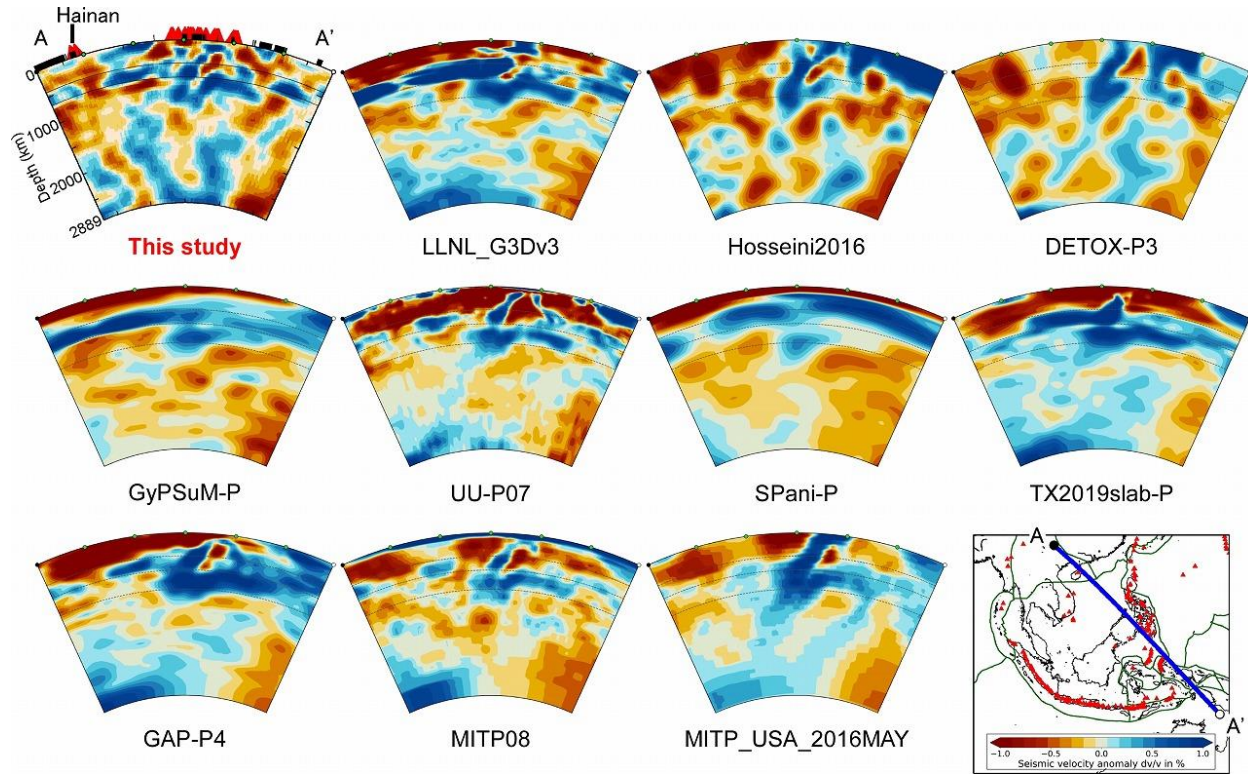
998

999

1000

1001

1002



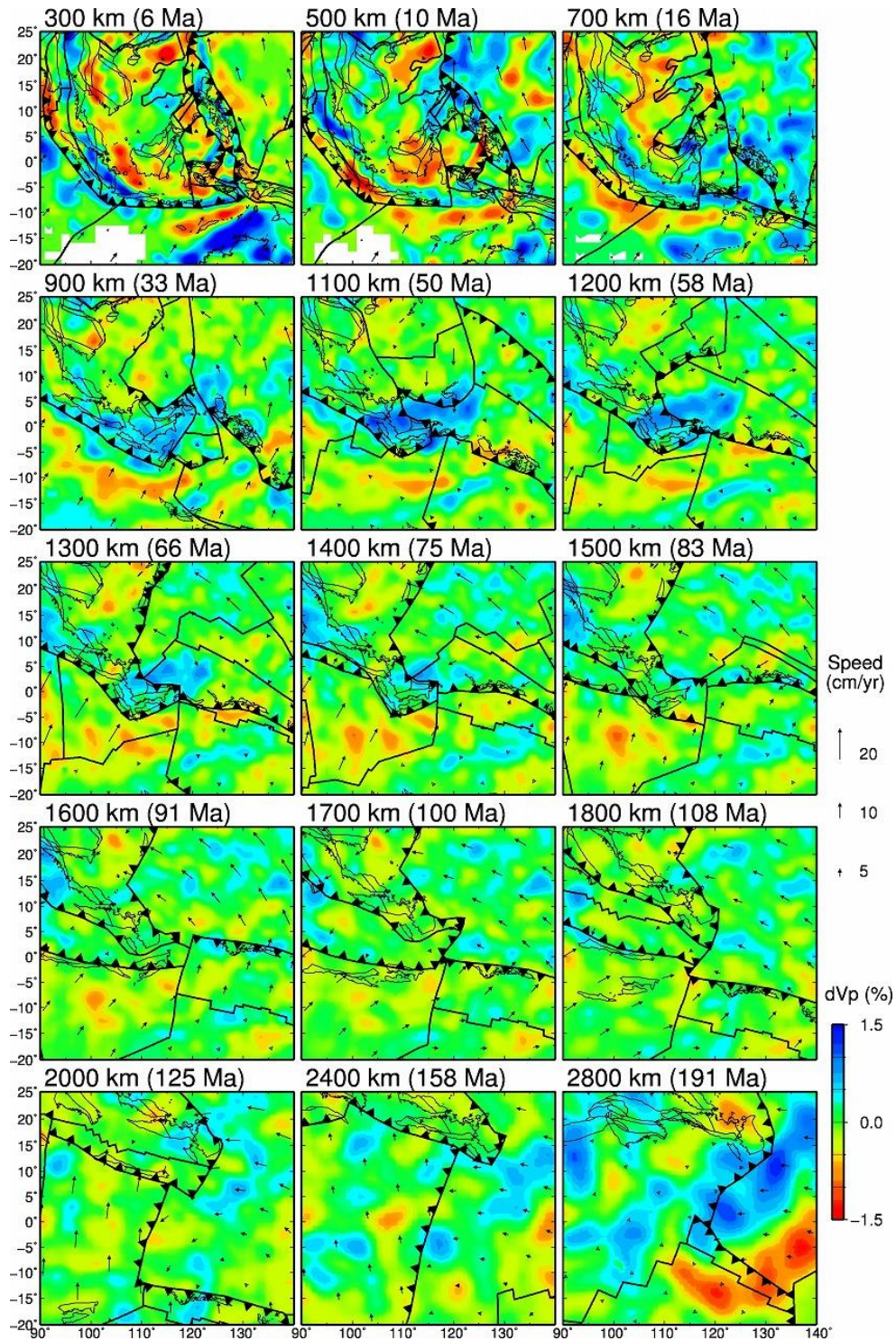
1003

1004 **Figure 13.** Comparison of a V_p vertical cross-section oriented in the NW-SE direction through
 1005 the Hainan hotspot obtained by this study (upper left) with 10 existing models, i.e., UU-P07
 1006 (Amaru, 2007), MITP08 (Li et al., 2008), GyPSuM-P (Simmons et al., 2010), LLNL_G3Dv3
 1007 (Simmons et al., 2012), GAP-P4 (Fukao & Obayashi, 2013; Obayashi et al., 2013), SPani-P
 1008 (Tesoniero et al., 2015), Hosseini2016 (Hosseini, 2016), MITP_USA_2016MAY (Burdick et al.,
 1009 2017), TX2019slab-P (Lu et al., 2019), and DETOX-P3 (Hosseini et al., 2020). All figures are
 1010 shown with the same color scale. The blue and red colors denote high and low V_p perturbations,
 1011 respectively, whose scale (in %) is shown at the bottom of each panel.

1012

1013

1014



1015

1016 **Figure 14.** Comparison of Vp map views obtained by this study with plate reconstructions
 1017 (Müller et al., 2019) using an age-depth relationship (Lithgow-Bertelloni & Richards, 1998). The

1018 thin black lines denote geological blocks. The thick black lines denote plate boundaries, among
1019 which the jagged lines are subduction boundaries. Thin arrows denote absolute plate motion
1020 direction and speed, whose scale (in %) is shown on the right.

1021

1022

1023

1024

1025

1026

1027

1028

1029

1030

1031

1032

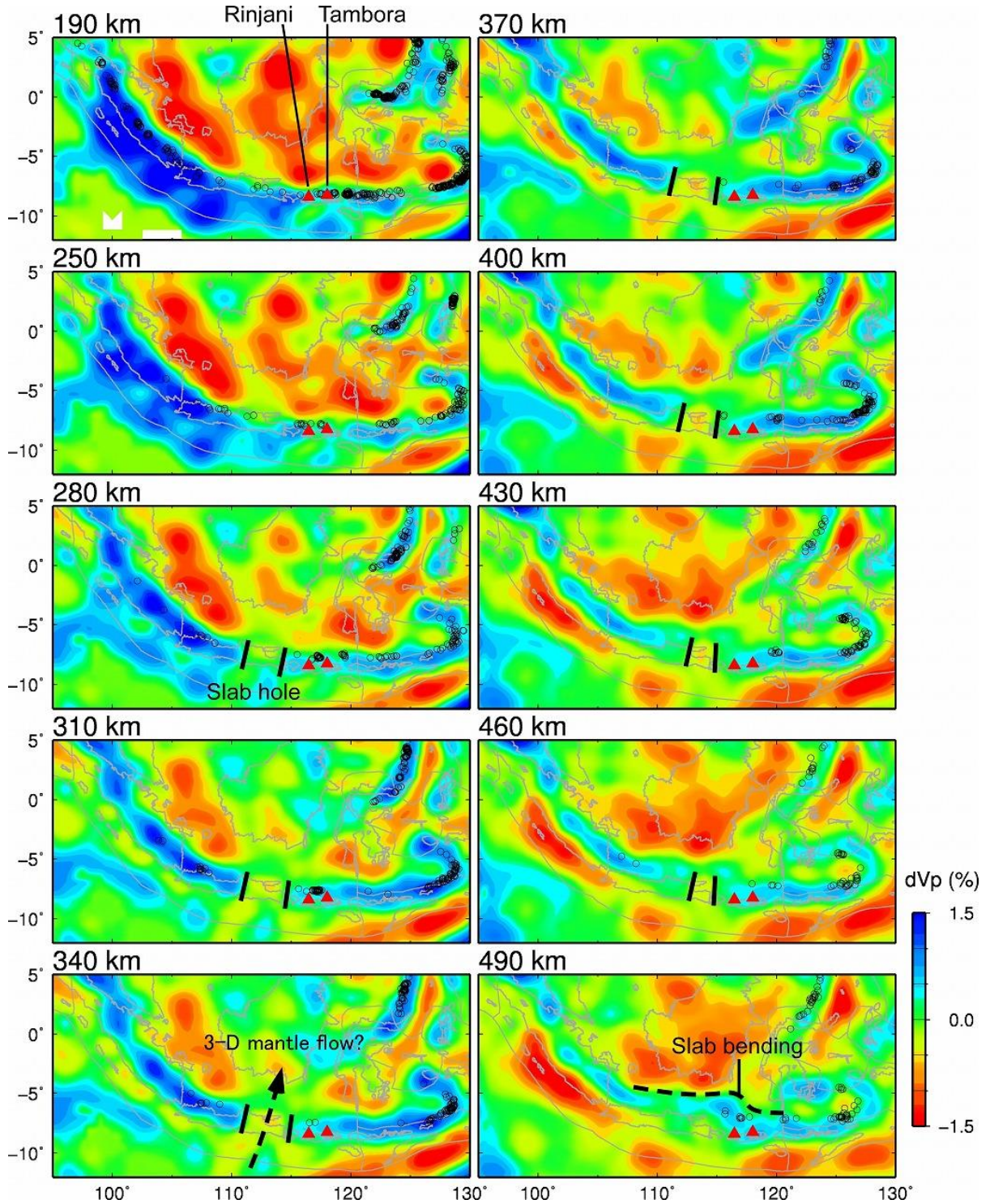
1033

1034

1035

1036

1037



1038

1039 **Figure 15.** Enlarged map views of Vp tomography at depths of 190–490 km around the
 1040 Australian slab. The layer depth is shown at the upper-right corner of each map. The blue and red

1041 colors denote high and low Vp perturbations, respectively, whose scale (in %) is shown on the
1042 right. Areas with hit counts < 50 are masked in white. The identified hole in the Australian slab
1043 is indicated in-between the two black solid lines. The red triangles denote the Tambora and
1044 Rinjani volcanoes, which are only two located in this region of the 25 world's volcanoes that
1045 caused large volcanic eruptions during the past 2500 years (Sigl et al., 2015). The open circles
1046 denote local seismicity within a ± 15 -km depth range of each layer.

1047

1048

1049

1050

1051

1052

1053

1054

1055

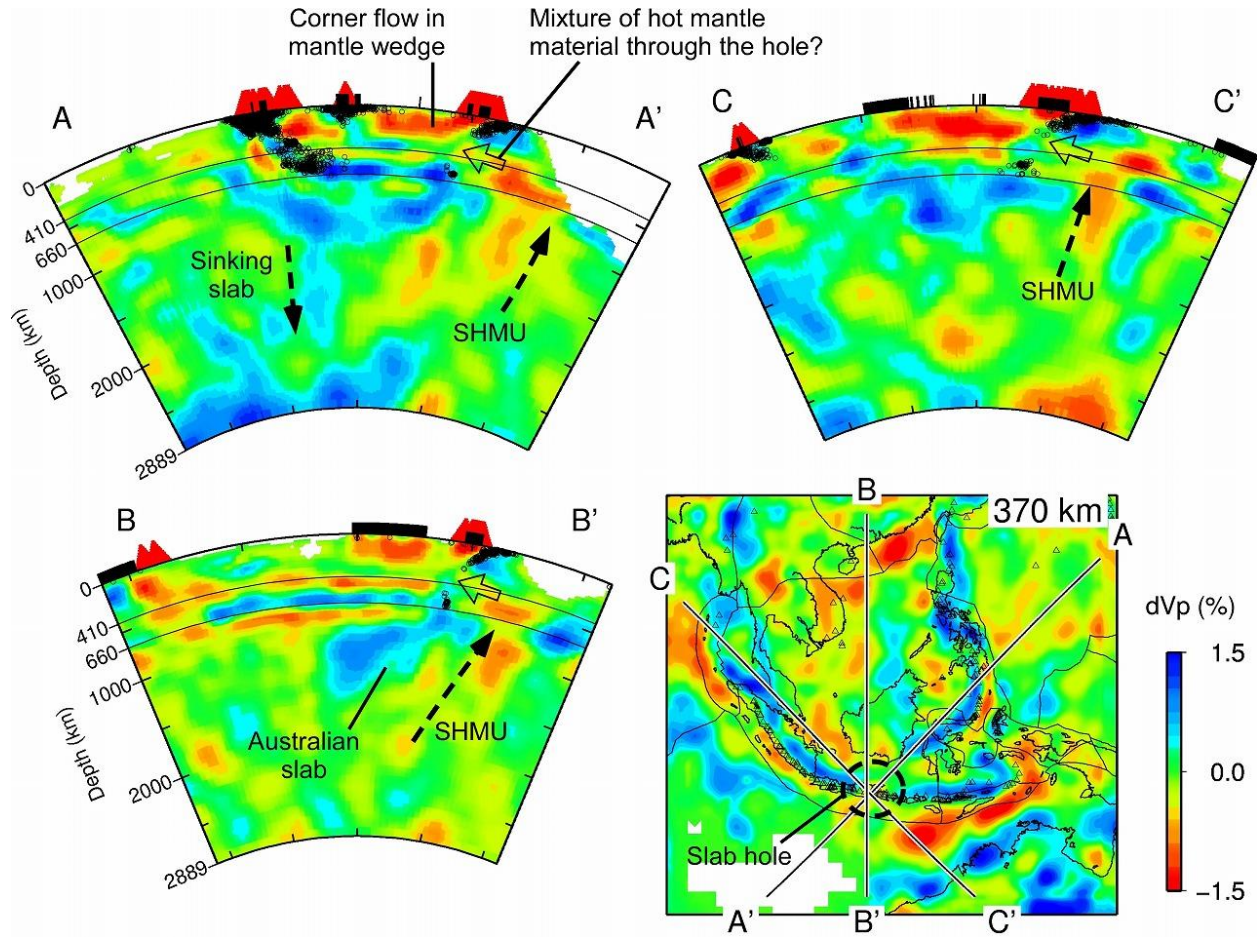
1056

1057

1058

1059

1060



1061

1062 **Figure 16.** Vertical cross-sections (A-A' to C-C') and a map view (lower right) through the hole
 1063 in the Australian slab beneath eastern Java. The red triangles denote active volcanoes within a
 1064 ± 222 km width of each section. The open circles denote local seismicity within a ± 111 km width
 1065 of each section. Locations of the profiles are shown on the map. The map view shows the
 1066 tomography at a depth of 370 km.